Electronic Technology Department

FINAL CAREER PROJECT

TELECOMMUNICATIONS ENGINEERING

Characterization of Integrable Photonic Sources of Pulsed Light via Mode-locked Ring Laser Diodes

Author: Álvaro Jiménez Galindo

Tutor: Guillermo Carpintero del Barrio

Leganés, December 2011

Título: Characterization of Integrable Photonic Sources of Pulsed Light via Mode-locked Ring Laser Diodes

Autor: Álvaro Jiménez Galindo

Director: Guillermo Carpintero del Barrio

EL TRIBUNAL

Presidente: Pablo Acedo Gallardo

Vocal: Ascensión Gallardo Antolín

Secretario: Luis Jorge Orbe Nava

Realizado el acto de defensa y lectura del Proyecto Fin de Carrera el día __ de _____ de 20__ en Leganés, en la Escuela Politécnica Superior de la Universidad Carlos III de Madrid, acuerda otorgarle la CALIFICACIÓN de

VOCAL

SECRETARIO   PRESIDENTE

Thanks

Es mucha la gente que comenzó esta carrera de fondo conmigo. Algunos se fueron definitivamente de mi vida, otros se apartaron temporalmente y solo unos pocos han permanecido a mi lado. Gracias Daniel por el cariño que siempre me has ofrecido sin pedir nada a cambio y por enseñarme más cosas de las que podría haber imaginado. Papá, muchas veces me quejaré de tus palabras o de tus despistes, pero tienes el corazón más grande que nunca he visto y no sabes lo que agradezco las eternas oportunidades que me ofreces. Y tú mamá me has enseñado a ser mejor en todos los aspectos para poder ser una persona feliz, ya que sin ti me habría ahogado muchas veces en mí mismo.

Los que ya estaban conmigo antes de empezar me ayudaron con mis agobios y me enseñaron lo bonito que es ser distintos, por eso no podré olvidar nunca a Adel, Almudena, Dani, Helena e Irene. Incluso mucha gente no llegará a leer esto, pero cada scout que ha pasado por mi vida ha dejado huella en mi corazón y me han enseñado a compartir y a disfrutar de las pequeñas cosas.

Ya en la universidad, un mundo nuevo para todos, no habría sido lo mismo sin Gonzalo, que siempre tuvo una sonrisa y tiempo para escuchar. Además no podría dejar de mencionar al equipo Porraskazo y cada uno de sus integrantes, con los que he disfrutado innumerables veces. Son muchos más los que fueron añadiéndose a la gran lista de compañeros y con los que espero no perder el contacto, pero no los nombraré aquí mismo porque no quiero dejar a nadie fuera.

Se incorporaron a mi vida también en esta etapa varias personas más, aunque merecen especial mención. Miriam, he aprendido mucho de tu energía y de tu carácter, que complementando tu sinceridad hacen de ti una de las personas más íntegras que conozco. Gracias Luis, Alex e Iván por acogerme como a uno más, por estar siempre a mi lado. Espero que esto solo haya sido el principio de todo lo que nos queda por vivir. Tú fuiste la última en llegar a mi lado, y aun así siempre has sido la más implicada a la hora de darme cariño, comprensión y ánimos. Mucha 'culpa' de mis últimos estupendos años la tienes tú, Alba.

Mi tutor fue una bendición para mí, ya que era el ideal con el que siempre había contado. Alguien que nos escuchara y, sobre todo, que nos enseñara a interesarnos y a crecer con la máxima ilusión por el trabajo que hacemos. Guillermo, no me cabe duda de que eres el profesor más importante que he tenido y quedas como un claro referente en mi etapa académica y profesional. Gracias por todas y cada una de las oportunidades que me has brindado.

Buena caza y largas lunas.

Resumen

El presente proyecto ha consistido en el estudio en profundidad de una serie de láseres en anillo enganchados en fase, integrados en una placa de circuito. Los láseres en anillo de semiconductor son una fuente atractiva de pulsos ópticos para los sistemas fotónicos integrados que necesitan componentes compactos y económicos, necesarios para un desarrollo comercial exitoso. Además, estos diodos láser pueden ser integrados junto con otros componentes ópticos en el mismo circuito, lo que reduce su tamaño, las pérdidas y el precio. El hecho de que sean láseres enganchados en fase contribuye a generar pulsos cortos de luz a una determinada tasa de repetición, por lo que los láseres de anillo son una gran fuente de luz para muchas aplicaciones, especialmente en el área de las comunicaciones.

Tres interfaces software han sido desarrollados para interactuar con los instrumentos presentes en el laboratorio para automatizar las medidas que se han tomado. El objetivo era medir parámetros típicos de los láseres en estudio: la curva de potencia óptica frente a la intensidad (curva PI), el espectro de radiofrecuencia junto con su ruido de fase y la autocorrelación de los pulsos de luz presentes en la guía onda de salida del láser. También se ha incluido la medida del espectro óptico para completar los resultados.

Los resultados obtenidos de la curva PI han permitido determinar la corriente umbral de los diodos láser en anillo y los distintos regímenes de trabajo. Las medidas del espectro óptico y de radiofrecuencia han contribuido a establecer la hipótesis de funcionamiento en modos enganchados en fase, y este hecho ha sido corroborado por el estudio de autocorrelación de los pulsos emitidos. Por último, algunos resultados muy interesantes pueden ser extraídos de estas últimas medidas sobre una estructura de anillo láser simétrico con dos secciones SOA y un absorbente saturable. En primer lugar, se ha corroborado que el régimen de modos enganchados en fase se induce a través de una polarización inversa en el contacto del absorbente saturable, apareciendo pulsos de luz ultracortos bien definidos. En segundo lugar, se ha demostrado que la forma y el ancho de estos pulsos se puede controlar a través de la polarización asimétrica de sus dos secciones de ganancia.

La tasa de repetición del láser simétrico es de 14,98 GHz y se han obtenido pulsos de entre 1 y 2 picosegundos de ancho temporal. Los mejores resultados incluso ofrecen un ancho de pulso temporal por debajo de 1 ps con un perfil lorentziano, que es un hecho muy interesante.

Abstract

The present project has consisted in the in-depth study of a series of mode-locked ring lasers integrated in a circuit board. Semiconductor ring lasers are an attractive source of optical pulses for photonic integrated systems which need compact and cheap components, required for a successful commercial development. Furthermore, these diode lasers can be integrated together with other optical components in the same circuit, thus reducing size, losses and price. Mode-locking contributes to generate short light pulses at a given repetition rate, making ring lasers a great source for many applications, especially in the communications area.

Three software interfaces have been developed to interact with the instruments present in the laboratory to automate the measurements that have been taken. The objective was to measure typical parameters of the lasers under study: the curve of optical power versus intensity (PI curve), the radio frequency spectrum together with its phase noise and the autocorrelation of the emitted light pulses at the output waveguide of the lasers. It has also been included the measurement of the optical spectrum to complete the results.

The obtained results of the PI curve have allowed determining the lasing threshold of the diode ring lasers and different working regimes. Optical and radio frequency spectrum measurements have contributed to establish the hypothesis of mode-locking functioning, and this fact has been corroborated by the autocorrelation study of the emitted pulses. Finally, some very interesting results can be extracted from these last measurements over a symmetric ring laser structure with two SOA sections and a saturable absorber. In first place, it has been corroborated that the mode-locking regime is induced through a reverse bias in the saturable absorber contact, appearing well-defined ultrashort light pulses. Secondly, it has been proved that the shape and width of these pulses can be controlled throughout the asymmetric biasing of its two gain sections.

The measured repetition rate of the symmetric laser is of 14.98 GHz and pulses between 1 and 2 picoseconds have been obtained. The best results even offer a temporal pulse width under 1 ps with a Lorentzian profile shape, which is a very interesting issue.

General Index

Figure Index

Table index

Chapter 1

Introduction to ring lasers

1.1. Introduction

Semiconductor lasers are considered to be the best light sources for high rate optical fibre communications as well as for signal processing systems due to a range of unique characteristics such as small size, high efficiency, low cost and possibility of modulating the light output at high frequency by directly introducing variations in the current that is injected to the device.

In optical fibre communications two multiplexing techniques are used to increase the transmission capacity: Wavelength Division Multiplexing (WDM) and Time Division Multiplexing (TDM). Nowadays, both are combined and each WDM wavelength establishes a transmission channel in which TDM is employed. Today's semiconductor lasers are capable of tuning their wavelength to adapt to WDM standards and allow the generation of ultrashort pulses at extremely high repetition rates to create the TDM signal. Moreover, they can also be modulated and encoded. Semiconductor lasers are the perfect candidates for these functions because of all the advantages that have been explained.

In addition, semiconductor ring lasers are an attractive source of optical pulses for photonic integrated systems which require compact and cheap components, required for a successful commercial development. The advantage of ring resonator lasers is that these can be easily integrated at any place in the chip since the feedback is achieved without cleaved facets or gratings. They operate in a single transverse and longitudinal mode without the need for accurate gratings or overgrowth and hence offer themselves strongly for low cost mass-production. Due to this interest, research on these devices has already demonstrated continuous-wave (CW) [1] and single-mode operation [2] two decades ago. However, ring

lasers were shown to operate with two counter-propagating modes in the ring resonator, the clockwise and the counter-clockwise modes. Modelocked operation was achieved shortly afterwards [3], [4], showing that the bidirectional light circulation of the device makes it particularly suited for colliding pulse mode-locked (CPM) operation.

In recent years, more techniques have been developed. Deeply etched waveguides are extremely important for photonic integrated circuits, as they push up the limits of these systems by achieving the integration of various components into a reduced area. Deep etching causes a strong lateral confinement of light, allowing for narrower waveguides which can have smaller bending radius, hence allowing to reduce the size of the photonic integrated circuits. Even with a very small radius (< 10 μm) they can be used for low-loss interconnection. Further, deep etched MMI-couplers and deep etched AWG's, key components in Photonic Integrated Circuits, can be made with lower dispersion of their performance characteristics than shallow etched ones [5].
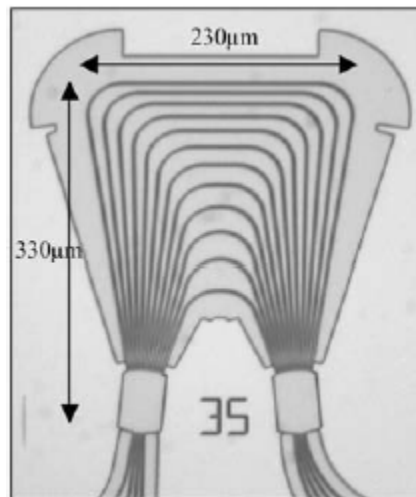
Figure 1. Deep etched InP-based AWG [5]
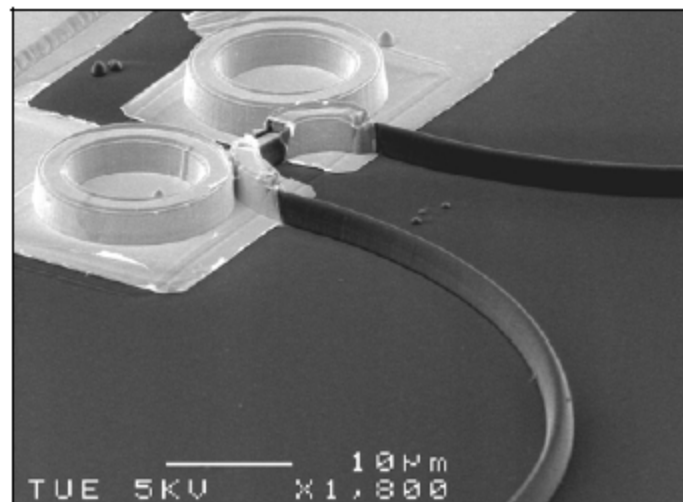
Figure 2. Basic elements in micro-electronic and micro-photonic integration [5]

In optical fibre communications two multiplexing techniques are used to increase the transmission capacity: Wavelength Division Multiplexing (WDM) and Time Division Multiplexing (TDM). Nowadays, both are combined and each WDM wavelength establishes a transmission channel in which TDM is employed. Today's semiconductor lasers are capable of tuning their wavelength to adapt to WDM standards and allow the generation of ultrashort pulses at extremely high repetition rates to create the TDM signal. Moreover, they can also be modulated and encoded. Semiconductor lasers are the perfect candidates for these functions because of all the advantages that have been explained.

1.2. Functioning principle

Lasers are basically oscillators which work at optical frequencies. The definition of an oscillator includes two fundamental elements, an amplifier and a feedback network.

1.2.1. Optical amplification

Amplification phenomena at optical frequencies are closely related to the transition processes of charge carriers (electrons and holes) between valence and conduction bands, and their iterations generating photons whose energy coincides with the gap's energy. Semiconductor lasers are devices in which these phenomena are produced when a P-N junction is directly polarized by an external voltage source, allowing the creation of an inverse population in the material (electrons in the valence band and holes in the conduction band). The bands' structure and iterative processes with the light in a semiconductor laser are shown in Figure 3.

(a) Absorption   (b) Spontaneous emission   (c) Stimulated emission
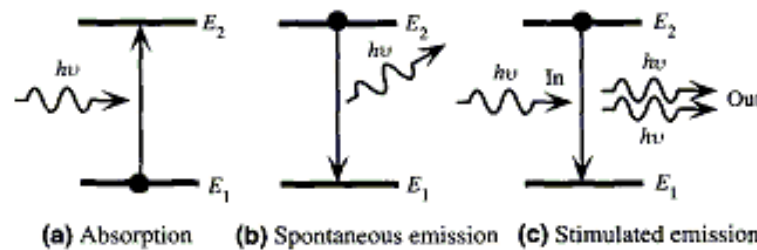
Figure 3. Radiative transitions in a semiconductor laser

The necessary condition for a transition between the valence and conduction bands is that the photon's energy checks the equation

$$h\omega = E_2 - E_1$$

where h corresponds to the Planck's constant, E_2 is the conduction band's energy and E_1 the valence band's energy. In Figure 3, three cases can be distinguished:

(a) Absorption. This process produces optical losses in the material. A photon that travels through the material is absorbed, producing the transition of an electron from the valence band to the conduction band.

(b) Spontaneous emission. No external factors are implied in this process, where an electron goes from the conduction to the valence band, releasing a photon.

(c) Stimulated emission. This effect is also known as laser effect, where a photon is released induced by another photon. If feedback and selectivity exist, coherent light emission is produced [6].

The stimulated emission case is formally a light amplification effect. Because of its existence together with absorption, only at certain limit the inverse population is achieved at which photon emission due to stimulated recombination overcomes the absorption produced by the hole – electron pairs generation. This inversion level is called transparency, as the material becomes transparent for light.

From this situation, the necessary condition for laser emission can be extracted; stimulated emission must overcome all the possible losses. Optical gain is directly related to the stimulated emission rate, is linearly dependent on the carrier concentration and varies parabolically with wavelength.

$$g = g_0(n - n_t) + b(\lambda - \lambda_p)^2$$

1.2.2. Feedback network

A feedback network for an optical resonator consists on the creation of a cavity in which the amplification will be produced, using mirrors to send part of the amplified light back into the amplifier. There are to main ways of achieving this.
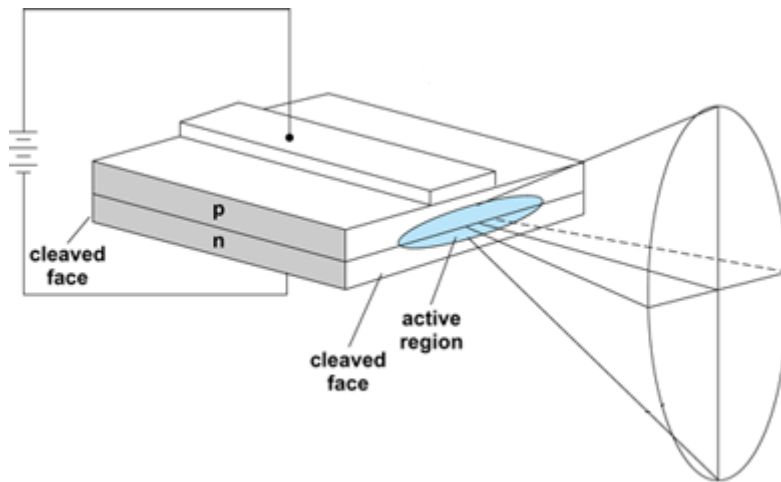
Figure 4. Monolithic laser cavity scheme

1.2.3. Fabry Perot resonator

The simplest mean to provide feedback is through a Fabry-Perot resonator, in which two parallel mirrors are created at the extremes of the gain medium by simply cleaving the two end facets of the semiconductor crystal in which the PN gain media is grown. Selectivity is achieved in a single direction and only photons which travel in that axis are reflected, acquiring maximum gain and contributing to the stimulated emission process. The length of the

resonator selects the emission frequency and the resonator's propagation must be compatible with the cavity modes [7].
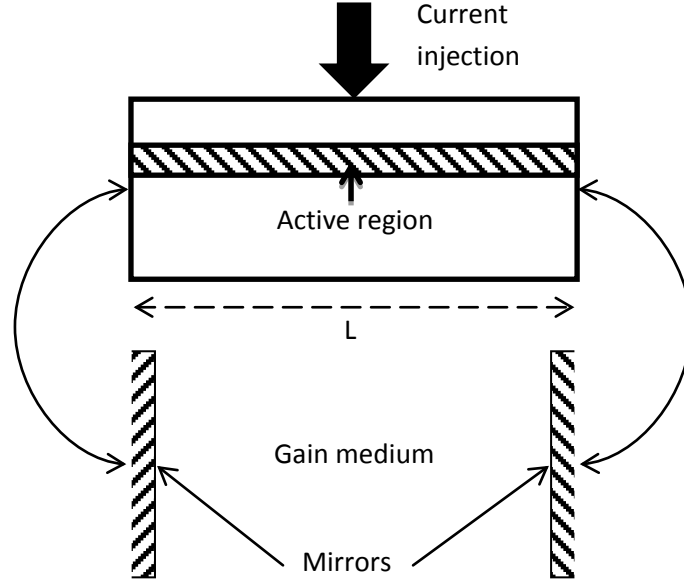
Laser emission, described by the gain g_m, begins when the internal losses α_i and the losses through the cavity facets α_m are surpassed. The field in the cavity will be described as a monochromatic plane wave, E^+ which propagates in the positive sense for z, and E^- in the negative direction, with a β propagation constant [8].

$$E^+(z) = E_0^+ e^{-i\beta z + \frac{1}{2}(g_m - \alpha_i)z}$$

$$E^-(z) = E_0^- e^{-i\beta(L-z) + \frac{1}{2}(g_m - \alpha_i)(L-z)}$$

Boundary conditions are applied:

$$E^+(z=0) = E_0^+ = \sqrt{R_1} E^-(z=0)$$

$$E^-(z=L) = E_0^- = \sqrt{R_2} E^+(z=L)$$

Oscillation condition in the cavity is given by:

$$R_1 R_2 e^{-2i\beta z + (g_m - \alpha_i)L} = 1$$

The threshold condition for laser emission can be derived from this last equation, taking its absolute value:

$$g_{m,th} = \Gamma g(N_{th}) = \alpha_i + \alpha_m = \alpha_i + \frac{1}{2L} \ln\left(\frac{1}{R_1 R_2}\right)$$

where N_{th} is the carriers' density in the threshold in which the gain overcomes the losses [9]. Additionally, taking the phase of the same equation, the phase condition can also be derived for laser emission in a cavity of length L:

$$\beta L = m\pi$$

being m an integer. The frequency of the longitudinal modes is then:

$$\varpi_m = \frac{m\pi c}{nL}$$

n is the refraction index of the active zone of the laser. The central emission frequency ϖ_0 is defined by the nearest longitudinal mode to the gain's maximum of the active medium [8]. This fact is of particular importance for this project, because the studied devices are pulsed at the difference of two consecutive longitudinal modes.

However, the method that has been developed implies integration problems due to the facet cleaving.

1.2.4. Ring resonator

Optical feedback can also be achieved by means of optical ring resonators, creating circular structures with high integration potential since they do not need the crystal edge to produce optical feedback and so the resonator's length can be established easily. Furthermore, they are particularly adequate to be integrated in optical circuits and are very promising in applications like wavelength filtering, allowing unidirectional regimes which determine the direction of the propagating photons, as well as in multiplexing and demultiplexing applications [10].
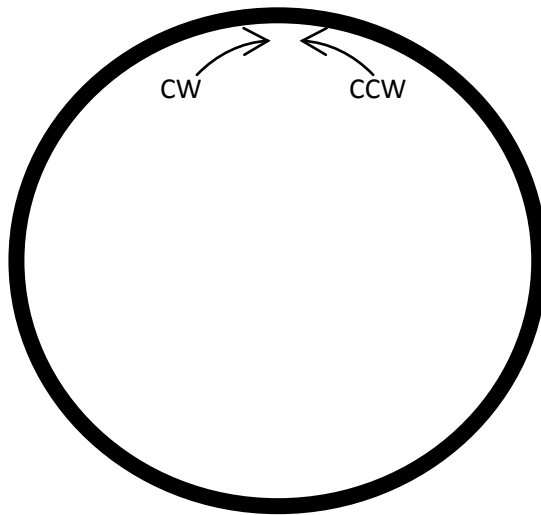
Figure 6. Ring laser scheme

1.2.5. Integrated optic beam splitters

Since ring lasers do not need cleaved facets to build the resonator, there is an issue of importance in the structure and it is how the optical output power is extracted from the ring. Output coupling of lasers has been widely studied and many investigations of branching waveguides have subsequently been pursued [11]. A variety of integrated optic beam splitters can potentially be used for splitting the optical power from the ring between the ring and an output waveguide. These splitters can be divided into five categories shown in Figure 7: the mirror splitter (a), the classic Y-junction splitter (b), the multimode interference (MMI) splitter (c), the branching ring laser with simple (d) or dual output (e) and the evanescent field coupler (f).

(a)	(b)	(c)	(d)	(e)	(f)
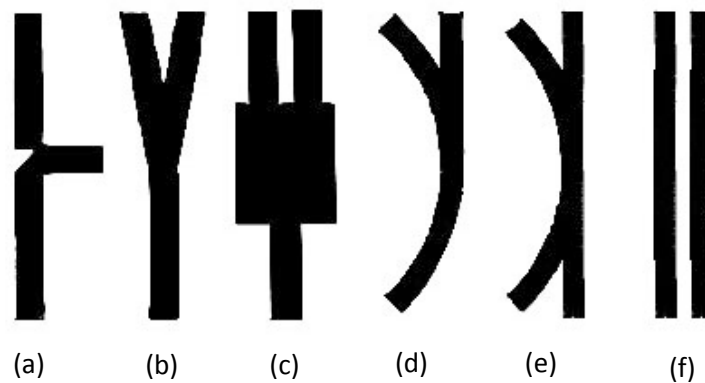
Figure 7. Waveguide couplers

A mirror splitter, shown in Figure 7.a acts like a partially silvered mirror and is nearly an ideal beam splitter in which modal properties are well conserved. However, it relates back to cavity etching, requiring relatively advanced processing capabilities, and it is not an ideal option [12]. The Y-junction splitter operates by adiabatically expanding the input mode to maximize the overlap with the two output guide modes and adiabatically splitting the mode between the two guides. The problem comes by the splitting angle required to achieve this expansion, which is difficult to satisfy for ring junctions with small radix. In addition, the field has its maximum at the vertex, and fabrication process variations due to the extreme sharpness of a small splitting angle must be expected. This leads to an extreme sensitivity to variations which is not desired. The multimode interference splitter operates by exciting multiple modes of the mode coupler region. As the modes propagate at different velocities, the field evolves until the resulting pattern matches the output waveguide modes so as to improve the coupling efficiency.

In the case of a ring laser being coupled into a straight guide, the fundamental mode of the ring laser, an edge guided mode, interferes with itself by interacting with the outside sidewall of the straight guide. A comparison can be established between the Y-junction and the straight guide coupling due to their geometrical similarities. This conversion results in the outgoing beam splitting into two beams so that there is little radiation loss at the junction vertex as it happens in the Y-junction. The last case corresponds to the evanescent field coupler, in which a certain portion of the original beam's energy will couple to the nearby

waveguide. The coupling coefficient can be varied, although it will also be extremely sensitive to the gap between both guides.

1.2.5.1.   Y-junction or straight guide couplers

The Y-junction or straight guide couplers are usually employed in semiconductor ring lasers because it is the most straightforward solution, generated by simply joining a tangential waveguide to the circular resonator. Such a junction splits the incoming beam into two output beams, one of which is fed back into the laser resonator [12]. Due to modal mismatch, a significant additional fraction is lost due to radiation and higher order modes that eventually radiate out. The splitting ratio is determined by the radius of the circular resonator, the waveguide width and its relative position with respect to the circular guide. Furthermore, the ratio can be changed with the position of the waveguides, favouring the feedback or the output excitations.

For the straight guide coupler with double output, the coupling ratio can be slightly different for the two lasing directions, which could be caused by small deviations of the fabricated structure from an ideal symmetric coupler such that the counterpropagating modes experience slightly different splitting ratios.

1.2.5.2.   Evanescent field couplers

Evanescent field couplers are very common elements in integrated optics, and are often used as 3 dB directional couplers. However, one the main problems related to these structures is the sensitivity of the coupling ratio to variations of the coupler dimensions, particularly the coupling gap. This situation makes it difficult to produce a given coupling ratio accurately and reproducibly.

Evanescent field couplers are important for some lasers, such as the twin coupled lasers, but are not so frequently employed in ring designs.
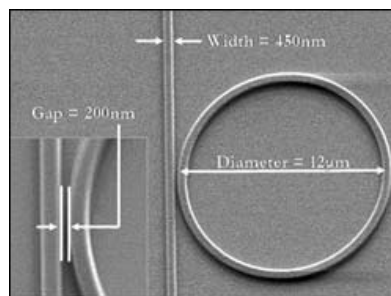
Figure 8. Evanescent field coupler

1.2.5.3.   MultiMode Interference (MMI) Couplers

MMI Couplers have attracted widespread attention, mostly because they allow increased fabrication tolerances compared to directional couplers, without compromising performance except with respect to cross-talk. Ring lasers have shown superior operation characteristics to devices with Y-junction or straight guide couplers [13] [14].
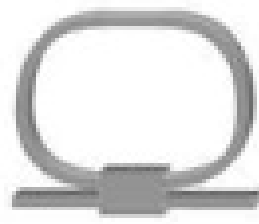
Figure 9. MMI coupler

In summary, semiconductor ring lasers with output coupling through MMIs are superior to those employing Y-junctions or directional couplers due to their improved performance and repeatability, since the coupling ratio in MMI couplers is very tolerant to changes in mode position, refractive index and wavelength that occur during operation. The same applies to fabrication tolerances, where small changes do not influence the device operation significantly [12].

Directional couplers do not offer the same fabrication and operational robustness. For example, the coupling ratio depends critically on both the etch depth and the separation of the two waveguides, and also changes with injection current. On the other hand, they offer a more compact means of extracting power because it is possible to couple directly out of a circular ring. Furthermore, the coupling ratio can be adjusted to any value, unlike the situation in interference devices, where only fixed coupling ratios are available. The adjustable coupling ratio is a very attractive feature, because it allows outcoupling of a high fraction of the available light to yield a higher differential efficiency [4]. However, the splitting ratio of a 2 x 2 MMI coupler can be varied in a well-controlled manner if the coupler is excited off-centre.

Y-junctions have the same problems of sensitivity to operational parameters as directional couplers, and the additional disadvantage of generating excess radiation loss and backreflections at the junction itself [15]. Hence, the popularity of these couplers is not so much satisfied by its performance as by its simplicity.

1.3. Mode-Locking Lasers

One of the main characteristics of mode-locking lasers is that they emit optical pulses at high rates instead of a continuous wave. There are a large number of applications in which these light sources can be used, extending to high rate optical communication systems and optical data processing [16]. For these fields, the generation of short pulses is an important issue in which lasers play a determining role. Between them, laser diodes present clear advantages with respect to other technologies, as they can be directly modulated up to tens of gigahertzs, reaching high repetition rates, a high efficiency and the possibility of developing integrated and compact solutions.

Among the main techniques of generating ultrashort optical pulses from laser diodes, there is mode-locking [17] which is the basis of this project. It is also applied to lasers based on other technologies. Its base is the control of the phase relation between the present modes in

the laser cavity. If these phase relations are kept locked, the optical power intensity presents a pulsed outline [8].

The theoretical base of mode-locking includes the gain of the material together with the cavity length of the device. As it was explained previously, laser modes are locked in phase and equally spaced. The material's gain bandwidth determines the number of modes that are present in the spectrum of the devices. To achieve an ideal pulse, the entire spectrum should be considered. However, the material is important in this place, as it will determine the quantity of modes with enough power to contribute to the pulse. In Figure 10 it can be seen that only a few modes will be kept in the laser due to the gain material. For a greater bandwidth, more modes will be included and the resulting optical pulse will be narrower.
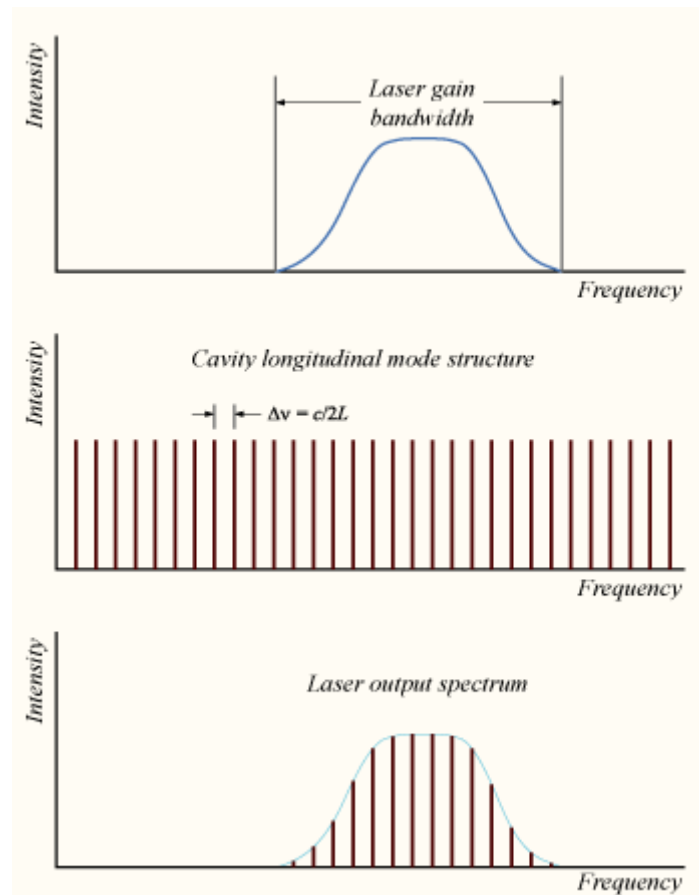
Figure 10. Effects of the laser's gain bandwidth

When the light sources for pulse generation are semiconductor mode-locked lasers, to the previously mentioned advantages it can be added their small size and their integration possibilities with other semiconductor elements.

Mode-locking regime is characterized by its constant phase relation between different modes of laser emission [18]. These devices have demonstrated the possibility to reach repetition rates up to 860 GHz, being usual to find devices up to 40 GHz due to the linear relationship between an increase in the frequency, costs and energy consumption [19]. These moderate repetition rates allow the synchronization of the pulse train with an electric signal, often finding channels operating at a 10 GHz rate [17].

The main applications in which mode-locked lasers are used are the optical communication networks based on optic time division multiplexing (OTDM). In contrast to the wavelength division multiplexing technique (WDM), OTDM allows to increase the number of channels without a rise in the technology costs and number of components, with their corresponding maintenance costs [20]. However, OTDM applications need a stable light source which generates optical pulses with low jitter [18] [21]. Recently, more application fields have appeared for mode-locked lasers, as optical signal processing and analogic to digital conversion.

Nowadays there are different techniques to lock lasers' modes. Specifically, the most interesting technique for the present project is passive mode-locking (PML). Its main advantage is that it does not require a radio-frequency (RF) signal to operate, being enough a constant voltage and current to operate the devices. Nevertheless, depending on the current and voltage levels applied to the device, it can present different working regimes. Additionally to the regime of interest in this project, it is usual to find two more regimes: *Q-switching* and *Q-switched Mode Locking* [22].

A brief description is now presented of the implicated processes in the mode-locking regime which allow locking phase modes by means of the passive mode-locking technique. Later, a series of characteristics of the other two regimes which are often found are presented.

1.3.1. Passive Mode-Locking (PML)

The key element to lock the modes in phase is the saturable absorber. For this reason, the device is formed by a gain region, to which the saturable absorber is added, and it is basically a P-N junction as the gain region of a semiconductor laser. While the gain region is polarized with a continuous current, the saturable absorber is polarized with an inverse constant voltage.

The development of the passive mode-locking between these two sections is illustrated in Figure 11. It is fundamental that the losses saturate faster than the gain, creating a time lapse in which the gain overcomes the losses giving the total system positive net gain and generating a light pulse. This is usually expressed as if the saturation energy of the saturable absorber must be smaller than the saturation energy of the gain section. If, additionally, the recovery time of the saturable absorber is shorter than the one of the gain, the losses will exceed the gain at every moment except for the time in which the optical pulse reaches its maximum [23].

En each round trip in the cavity, the combined action of the saturation of the gain and losses influences in the optical pulse's shape, amplifying the maximum peak of the pulse and attenuating the lateral ends. This produces a net effect of reduction of the pulse's time width that is compensated in the stationary regime by widening mechanisms as the dispersion [24]. The minimum pulse width is limited by the gain bandwidth and the non-linear effects [10].
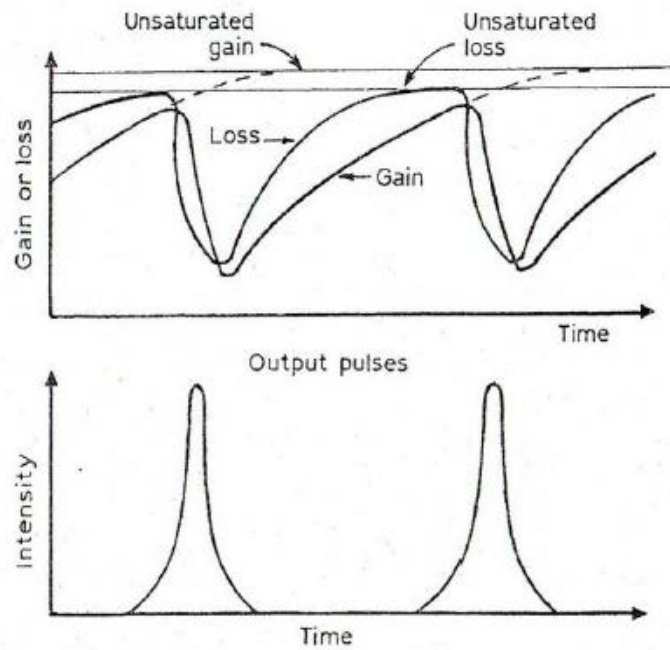
Figure 11. Passive Mode-Locking

As it has been previously commented and it can be observed in Figure 11, the mode-locked oscillations generate important variations in the gain and losses during the lapse of time in which the pulse passes. Hence, it is desirable that the repetition rate of the pulses is of the time order of the recovery time of the gain or losses. Additionally, and due to the reason that the device must start automatically the mode-locking, the maximum value for the gain must be higher than the maximum value of the losses [23].

The main difference between PML and the following regimes is that the repetition rate of the pulses is determined by the length of the cavity, which is a controllable physical parameter.

1.3.2. Q-switching

Historically, it was the first technique employed to generate ultrashort light pulses, and it is based in the change of the quality factor Q by means of the introduction of a variable attenuator. While the Q factor is low, losses are high enough to block the stimulated emission phenomenon, and therefore the laser emission. In consequence, an increase of the cavity's energy is produced. When, in a determined instant, the Q factor is changed, the energy stored exceeds significantly the losses and an intense light pulse is then released.

If the Q factor switching is produced externally, it is then denominated *active Q-switching*, and if a saturable absorber is also involved in the process, *self Q-switching*. One of the main requisites of the saturable absorber is to have linear absorption at the laser's wavelength. Hence, semiconductor lasers are remarkable due to the possibility of incorporation of a saturable absorber in the same material in which the active region of the laser is found. This situation contrasts with other laser types because of the need of an external saturable absorber [23] [25].

This regime is usually avoided because of its nature. Spontaneous emission is not easily managed and the repetition rate of the pulses cannot be controlled.

1.3.3. Q-switched Mode Locking

This technique is a combination of the two previously mentioned. Mode-locking frequency, given by the inverse of the propagation time through the laser cavity, is modulated with the Q-switching oscillation frequency, owing to dynamic instabilities [25].

Passive mode-locking lasers present two major disadvantages: high jitter and a difficult synchronization with external clock sources. These problems have led to the development of the technique called *Hybrid Mode-Locking* (HML), in which an electric clock signal is introduced in the saturable absorber [26]. In this way, the resulting repetition rate is synchronized with the injected RF signal. It should not be confused with the *Gain-switching* technique, which in contrast to other ultrashort pulse generating methods, does not need any special section in the device. Pulses are generated by the injection (by means of an RF generator) of a great quantity of electrons in the active region of the device, surpassing the laser's carrier threshold. When the threshold is reached, stimulated emission appears. However, as the stimulated emission appears faster than the carrier injection, their density falls under the threshold and no more light is emitted. If the electron injection continues, the process is repeated [23] [25].

Although Gain-switching and HML introduce an RF signal in the device, their function is totally different. In the first case, the RF signal determines the instants in which a high number of carriers are injected, but each burst does not emit light in the same period of time. Therefore, the RF signal does not establish de optical pulse rate at the output of the device. Instead, for HML, modes keep locked in phase and the RF signal determines the repetition rate of the output optical pulses.

1.4.   Mode-Locking Ring Lasers

There are various possible configurations for a passive mode-locking device. Between them, it is important to include the ring configuration, as it presents significant benefits compared with the Fabry-Perot lasers. While in this last configuration the cavity is defined by the mirrors that form the cleaved faces of the semiconductor material, ring lasers are conformed by a circular waveguide. The fact is very important because a fundamental factor can be controlled: the length of the optical resonator can be fixed by photolithography and so, the repetition rate of the pulsed light. It is defined by the cavity length; for the Fabry-Perot resonator the repetition time is R=1/2L, while in a ring laser it is R=1/L, being L the resonator's length. Ring lasers exhibit a better control of the repetition rate with respect to linear lasers [22].

Another important advantage of ring lasers is that they can be integrated with other optical components, creating a Photonic Integrated Circuit (PIC). The ring structure does not find the limitations imposed by the cleavage of the facets to create the mirrors. Moreover, it was this limitation that raised the need of new optical feedback methods. Between these solutions, the ring resonator was particularly outstanding [1].

Ring lasers present a distinctive characteristic. In the cavity, two modes are propagated in opposite directions. On one hand, there is the clockwise mode and on the other, the counter-clockwise mode. It is usual that both modes compete with each other, giving different possible situations of operation in the ring laser [22]. In cases where the ring resonator is an active cavity, it has been observed that the light direction can be controlled by injecting current in the laser's contacts [27].

Mode-locking ring lasers typically operate in a colliding pulse mode and support two counterpropagating fields in the cavity. In this regime, the CW and CCW light pulses reach the saturable absorber at the same time, supporting the two modes as it can be seen in Figure 12. However, for many applications it is desired unidirectional operation to have the most output power into one waveguide.
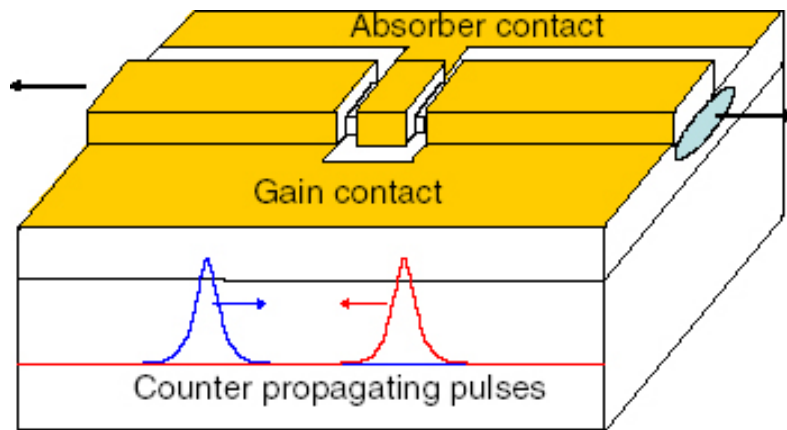
Figure 12. Colliding Pulse Mode-Locking [26]

The other option is the presence of a directional output with significant differences in the output power. The CW or CCW clearly overcome the one of the opposite direction, having a pure laser spectrum with one dominant mode versus another one with less power [27].
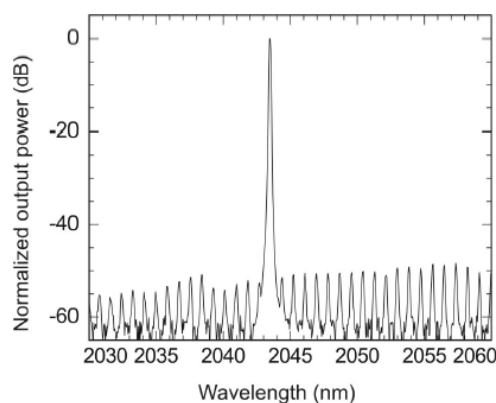
Figure 13. Laser spectrum for monomode emission [28]

For the present project, the measured curves show Colliding Pulse Mode-Locking (CPML), reaching the pulses to the saturable absorber at the same time. This implies that the energy of each pulse needed to saturate de absorber is reduced to the half, producing

additionally a pulse temporal compression. Results under one picosecond have been measured in this project.

As it has been explained before, ring lasers consist of a circular waveguide so there are no losses associated to mirrors. However, to extract light from these devices it is necessary to include a structure which allows the output of the light. This element, as well as its position with respect to the rest of the elements of the cavity influence deeply in the operation characteristics of the laser [10] [29]. When the arrangement of the different elements in the ring laser is such that the two counterpropagating pulses find the same optical path, the structure is known as *symmetric*. If not, *asymmetric*.

In the present project, both types of lasers have been measured. A single chip containing eight laser devices was employed. Figure 14 shows the modelled symmetric lasers under study, which show two amplifying sections, a saturable absorber and a multi-mode interference coupler. There are two identical paths for the pulses, which reach the saturable absorber at a time [22].
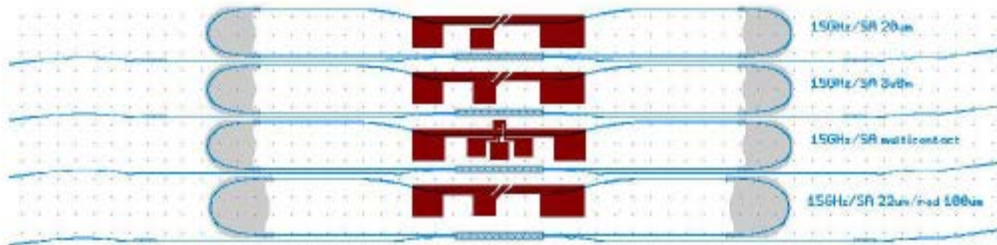
Figure 14. Symmetric ring laser models

Asymmetric ring lasers can also have various designs, but here are presented the lasers studied throughout the project. Optical paths are different for each propagating mode and two sections can be distinguished. Looking at Figure 15, it can be seen that the two upper lasers dispose of a total of four amplifying sections with two saturable absorbers, while the other two ring lasers have two amplifying sections and two saturable absorbers.
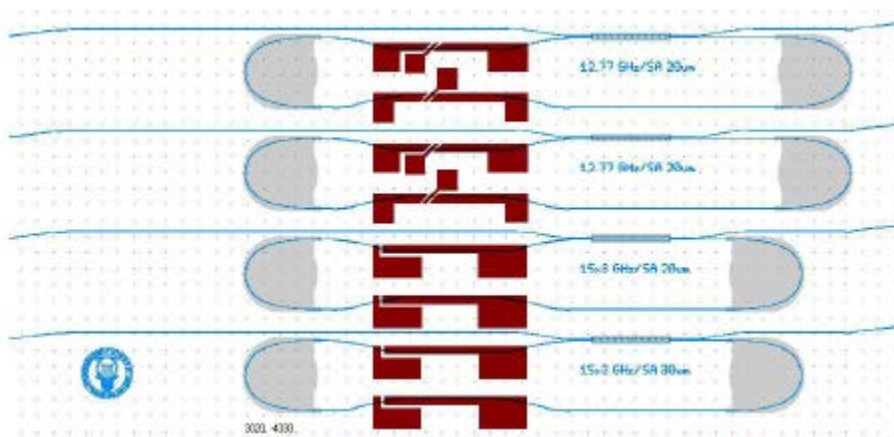
Figure 15. Asymmetric ring laser models

1.4.1. Characterization of mode-locked regime

An optical pulse with a pulse width of the order of picoseconds requires a detector bandwidth of several hundreds of gigahertz to recover appropriately the pulse shape. A low detection bandwidth leads to a broadened pulse envelope, limiting the resolution of the detector. For pulse width measurements, devices are available such as electrical sampling oscilloscopes, streak cameras, optical sampling oscilloscopes and autocorrelators.

The bandwidth of fast sampling oscilloscopes is limited due to the required optical-electrical signal conversion. Optical pulses of a full width half maximum (FWHM) of 1 picosecond, measured with a photodiode and an electrical sampling oscilloscope show a trace with a pulse width of approximately 10 picoseconds. Another problem arises from the accuracy of the time axis. It limits the resolution of the exact pulse position.

The temporal resolution of streak cameras is limited to 200 femtoseconds. Therefore a measurement of a 1 picosecond pulse would deliver only 5 measurement points. For shorter pulses, e.g. 400 fs pulses for 640 Gbit/s OTDM applications, the situation would be even worse. Furthermore, streak cameras need a great amount of power and can become a problem to measure some laser devices.

An alternative to the bandwidth limitation of photo detectors is the application of the pulse sampling based on an optical sampling system [30]. Another possibility to measure the pulse width is the commonly used intensity autocorrelation, which is the method selected for this project. A description of this technique is made in this chapter.

1.4.2. Pulse autocorrelation

An autocorrelator is an instrument in which the input signal is delayed and multiplied by the undelayed signal, the product of which is then smoothed in a low-pass filter to give an approximate computation of the autocorrelation function. It is used to detect non-periodic signals or weak periodic signals hidden in noise [31]. In this case, the autocorrelation is carried out through an APE Photonics system which uses interferometry to detect autocorrelation of optical beams.

1.4.2.1.   Theory of autocorrelation

When working with signals, cross-correlation is a measure of similarity of two waveforms as a function of a time displacement of one of them. It is also known as *sliding dot product* or *sliding inner-product* [32]. Mathematically, the cross-correlation of two complex square integrable functions $f(x)$ and $g(x)$ is defined as:

$$(f \star g)(x) \equiv \int_{-\infty}^{\infty} f^*(\tau)g(x+\tau)d\tau$$

where $f^*(x)$ is the complex conjugate of $f(x)$. If $g(x) = f(x)$, it becomes the cross correlation of $f(x)$ with itself, also called the autocorrelation, $A_f(x)$:

$$A_f(x) = \int_{-\infty}^{\infty} f^*(\tau)f(x+\tau)d\tau$$

$$= \int_{-\infty}^{\infty} f^*(\tau - x)f(\tau)d\tau$$

The most important properties of the autocorrelation function are:

- It is symmetric.

For real functions, it can be easily demonstrated:

$$A_f(-x) = \int_{-\infty}^{\infty} f(\tau - (-x))f(\tau)d\tau$$

$$= \int_{-\infty}^{\infty} f^*(\tau + x)f(\tau)d\tau = A_f(x)$$

- The function's maximum is always located at $x = 0$.

$$A_f(x = 0) = \int_{-\infty}^{\infty} |f(\tau)|^2 d\tau$$

As a result of the Cauchy-Schwarz inequality, this is the maximum possible value for $A_f(x)$.

- If $f(x)$ is periodic, $A_f(x)$ will also be periodic with the same period.

Being $f(x)$ periodic such that:

$$f(x + 2n\pi x_0) = f(x)$$

where x_0 is the period and $n \in \mathbb{N}$, then:

$$A_f(x + 2n\pi x_0) = A_f(x)$$

- The autocorrelation $A_h(x)$, with $h(x) = f(x) + g(x)$, is the sum of their autocorrelations plus the cross-correlation of the two functions.

$$A_h(x) = \int_{-\infty}^{\infty} h^*(\tau - x)h(\tau)d\tau$$

$$= \int_{-\infty}^{\infty} [f^*(\tau - x) + g^*(\tau - x)][f(\tau) + g(\tau)]d\tau$$

$$= \int_{-\infty}^{\infty} f^*(\tau - x)f(\tau) + g^*(\tau - x)g(\tau) + f^*(\tau - x)g(\tau) + g^*(\tau - x)f(\tau)d\tau$$

$$= A_f(x) + A_g(x) + (f \star g)(x) + (g \star f)(x)$$

The autocorrelation discards any phase information, returning only the squared magnitude of the function, evident in the $f^*(\tau + x)f(\tau)$ term. Taking this into account, this is

a non-reversible operation, not being possible to infer the original function without any additional information.

1.4.2.2. Electric field

Light is described by the electric field $E(r, t)$, which depends both in space and time. As we are interested in its temporal properties, only its time dependence will be studied. It is usually convenient to express the electric field as the product of an amplitude function and a phase term:

$$E(t) = \varepsilon(t)\left(e^{i(\omega_0 + \phi(t))} + e^{-i(\omega + \phi(t))}\right)$$

where $\varepsilon(t)$ is the electric field amplitude, ω_0 the carrier frequency of light and $\phi(t)$ its time dependent phases. If the field envelope and the time dependent phase terms are slow varying functions compared with the period of the carrier frequency, we can describe the light satisfactorily by these two terms. Intensity of the electric field is:

$$I(t) = \frac{1}{2}\epsilon_0 cn\varepsilon(t)\varepsilon^*(t) \propto |\varepsilon(t)|^2$$

where the physical constants are ignored. For a pulse of light, the pulse duration, τ_p, is usually taken as the full width half maximum (FWHM) of the intensity profile.

By means of the Fourier transform, the electric field can also be defined in the frequency domain:

$$E(\Omega) = \mathcal{E}(\Omega)e^{i\Phi(\Omega)}$$

The Fourier transform of the intensity is the spectral intensity:

$$S(\Omega) \propto |\mathcal{E}(\Omega)|^2$$

Similar to the pulse duration, the spectral width, $\Delta\omega_p$, is the FWHM of the spectral intensity profile. The pulse duration-bandwidth product is:

$$\tau_p \Delta\omega_p \geq 2\pi K$$

where K is a numerical constant that depends on the pulse shape. Values for common field envelopes are given in Table 1. Typical analytical functions for this pulsed light arise when solving Maxwell's equation with a particular set of boundary conditions, are the Gaussian and squared hyperbolic secant.

1.4.2.3. Optical Autocorrelation

Optical autocorrelation can be measured in various ways. The simplest one is the field autocorrelation where the electric field, $E(t)$, is what we are interested in. It is a time function, so it can be expressed the following way:

$$A_E(\tau) = \int_{-\infty}^{\infty} E(t)E^*(t - \tau)dt$$

The field autocorrelation is also known as first order autocorrelation, and it is referred to the spectrum of the signal by a Fourier transform:

$$S(\Omega) = \mathcal{F}\{A_E\}$$

The intensity autocorrelation can also be measured experimentally:

$$A_c(\tau) = \int_{-\infty}^{\infty} I(t)I(t-\tau)dt$$

It is usually known as the second order autocorrelation. Higher order autocorrelations for intensity are also possible, being the new definition:

$$A^{(n)}(\tau) = \int_{-\infty}^{\infty} I(t)I^n(t-\tau)dt$$

For a reasonably peaked function, and n being large enough, I^n behaves like a delta function, $\delta(t)$. A cross-correlation of any function with this delta is simply the function itself and hence $A^{(n)}$ is the same as the shape of the pulse.

However, determining the pulse width from the intensity autocorrelation, $A_c(\tau)$, requires some previous assumption about the pulse shape. If a pulse shape is assumed, the autocorrelation width, τ_{ac}, is related to the pulse width by a deconvolution factor k [33].

$$\tau_{ac} = \frac{1}{k}\tau_p$$

Commonly studied shapes have the deconvolution factors presented in Table 1.

Table 1. Values of *k* for different pulse shapes

Function	$I(t)$	k
Square	$I(t) = 1; \; |t| \leq T/2$ $I(t) = 0; \; |t| > T/2$	1
Gaussian	$I(t) = e^{-x^2}$	0.7071
Hyperbolic Secant	$I(t) = \text{sech}^2(x)$	0.6482
Lorentzian	$I(t) = \dfrac{1}{1+x^2}$	0.5000
Exponential	$I(t) = e^{-2|x|}$	0.4130

$\forall x = t/T$

1.4.2.4. Autocorrelation signals

There are different ways in which the autocorrelation is measured. To begin with, the basic principle of the autocorrelation techniques is shown in Figure 16. This autocorrelator

consists of a Michelson interferometer, a nonlinear crystal in which the second harmonic is generated and a linear detector (PMT - Photomultiplier). This crystal can be eliminated and use a nonlinear detector instead, but the result will be similar.
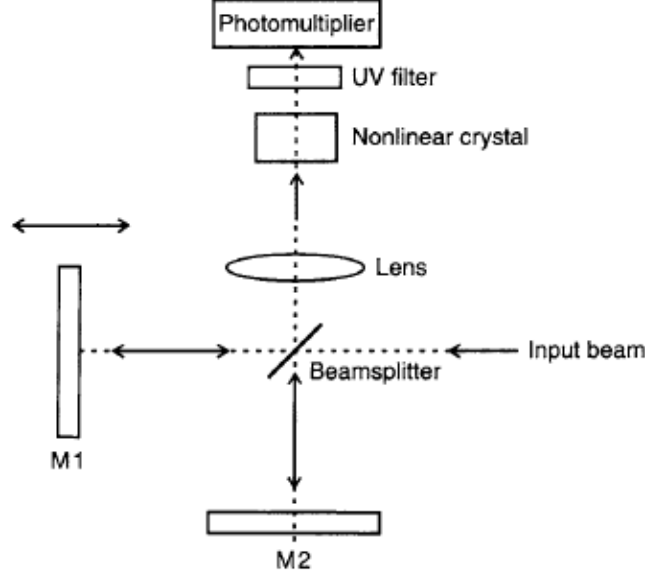
Figure 16. Diagram of the autocorrelator for collinear beams

The input beam, at frequency ω, is split into two identical beams. Each one of these beams passes through different optical paths in the two arms of the interferometer. The optical path in one of the arms can be changed by moving the mirror M1. This movement generates the delay time between the replica pulses. Without the nonlinear medium, the interferometric output that reaches the linear detector in Figure 16 is given by the intensity $I_1(\tau)$ as a function of the delay τ

$$I_1(\tau) = \int_{-\infty}^{\infty} |E(t) + E(t - \tau)|^2 dt$$

where $E(t)$ is the electric field of the laser pulse, as it was defined before. This can be expressed as a sum of the constant background contribution independent of the delay τ due to the intensities of the individual pulses and the first-order autocorrelation function $G_1(\tau)$

$$I_1(\tau) = \int I(t)dt + \int I(t - \tau)dt + 2G_1(\tau)$$

where

$$G_1(\tau) = \int_{-\infty}^{\infty} E(t)E(t - \tau)dt$$

However, this first-order autocorrelation function $G_1(\tau)$ does not yield a unique solution for the temporal pulse duration. For this reason, higher order autocorrelations generated by instantaneous optical nonlinearities are used in measurements. The most commonly used

nonlinearity is the second harmonic generation (SHG), as it has been done in the experimental setup of this project. If the two pulse replicas overlap in an SHG crystal, the signal is

$$I_{2\omega} \sim \int_{-\infty}^{\infty} |(E(t) + E(t-\tau))^2|^2 dt$$

Therefore

$$I_{2\omega} \sim \int_{-\infty}^{\infty} \left| \{A(t)e^{i(\omega t + \phi(t))} + A(t-\tau)e^{i(\omega(t-\tau)+\phi(t-\tau))}\}^2 \right|^2 dt$$

$$= \int_{-\infty}^{\infty} |2A^4(t) + 2A^2(t)A^2(t-\tau)$$
$$+ 4A(t)A(t-\tau)[A^2(t) + A^2(t-\tau)]\cos[\omega\tau + \phi(t) - \phi(t-\tau)]$$
$$+ 4A^2(t)A^2(t-\tau)\cos[2(\omega\tau + \phi(t)) - \phi(t-\tau)]| \, dt$$

where $A(t)$ and $\phi(t)$ are the time-dependent amplitude and phase, respectively. This expression contains the constant τ independent background and the part that is τ dependent. This part becomes much simpler after averaging over the delay time in the detector. It is automatic because the delay is fast enough in comparison with the detection time constant. Therefore, the autocorrelation signal becomes directly proportional to the second-order autocorrelation function $G_2(\tau)$ given by

$$G_2(\tau) = \int \frac{I(t)I(t-\tau)dt}{|I^2 dt|}$$

The constant background can be removed by non-collinear geometry of the Michelson interferometer presented in Figure 17.
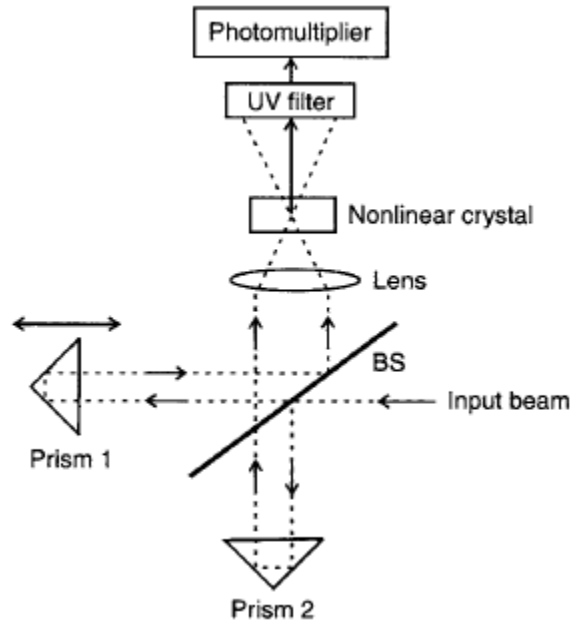
Figure 17. Diagram of an autocorrelator for non-collinear beams

The shape of the autocorrelation signal intensity profile depends on the shape of the pulses of the beams and is a function of the delay time. Mathematically, this operation is called *convolution*

$$G(\tau) = \int_{-\infty}^{\infty} I(t)I(t-\tau)dt$$

Once the intensity profile is obtained from the autocorrelator, a model is adjusted to the measurements that have been taken. A theoretically modelled pulse autocorrelation is then compared with the obtained trace, superposing different models and searching the one that fits better through the squared error. Table 2 shows the autocorrelation models for the three studied pulse profiles.

Table 2. Autocorrelation models for various pulse shapes

Function	$G_2(\tau)$
Square	$G_2(\tau) = 1 - \lvert y \rvert;\ \lvert \tau \rvert \leq T$ $G_2(\tau) = 0;\ \lvert \tau \rvert > T$
Gaussian	$G_2(\tau) = e^{-y^2/2}$
Hyperbolic Secant	$G_2(\tau) = \dfrac{3}{\sinh^2(y)}[y \coth(y) - 1]$
Lorentzian	$G_2(\tau) = \dfrac{1}{1 + (y/2)^2}$

$$\forall y = \tau/T$$

Chapter 2

Instrumentation and interface development

A set of ring lasers has been developed in the context of a more general project. To characterize them, three different interfaces have been developed so the measurements are automated in the laboratory.

The first one obtains a fundamental parameter of these devices: the threshold current. Additionally, the two outputs of each laser can be compared in the same graphic. In second place, the radio frequency spectrum is obtained together with the single side band (SSB) noise to analyse the repetition frequency of the optical pulses. Lastly, the laser pulses are studied by an interface which acts with the autocorrelator.

2.1. P-I-V characterization

The P-I (Power versus Intensity) curve is one of the most important parameters of any laser diode. From this curve, the threshold current can be derived, point from which the laser initiates the stimulated emission. Moreover, the quantic efficiency is given by the curve's slope.

In order to take the necessary measurements, three different instruments are managed in the setup of Figure 18:
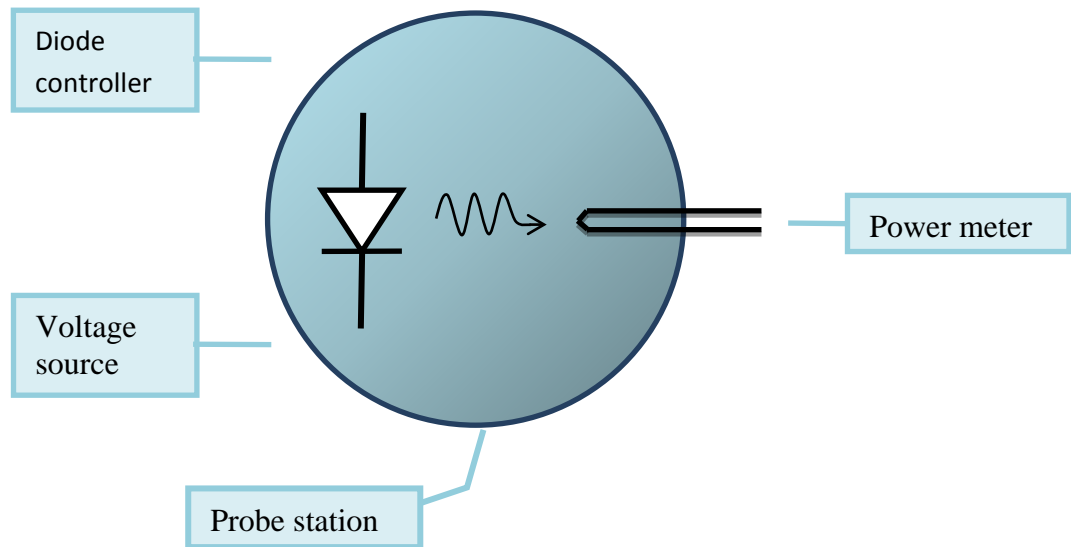
Figure 18. Setup for the P-I characterization

2.1.1. Laboratory Instruments

A brief description is made of the instruments involved in the development of each of the interfaces. For the P-I-V Characterization Interface, three instruments are included. Further on, only the new instruments will be described.

2.1.1.1.   Diode controller

Laser diodes emit light by providing them electrical current. This optical power depends not only on the current but also on the temperature of the device. For this reason, a diode controller implements a current source together with a temperature controller, compatible with thermistors, IC, and RTD temperature sensors. An automatic progressive variation of the output current protects the laser devices under test from abrupt changes which could deteriorate them.

The laser diode controller LDC 3724B present in the laboratory is managed by GPIB and the standard IEEE-488. In most of the experiments, a second laser diode was necessary, so it was used a Thorlabs instrument to inject a fixed current. This source was not controlled remotely.

Figure 19. Laser Diode Controller ILX LDC 3724B

2.1.1.2. Voltage Source

The lasers that have been measured for this project have a section of SA (Saturable Absorber). To do a complete characterization of the PI curve, voltage values in this section are needed and it is very important to have a stable voltage source to increase the devices' lifetime. In the laboratory, a HP E3631A voltage source is used.

Figure 20. HP E3631A Voltage Source

2.1.1.3. Optical power meter

One of the most important measurements made in this project is the PI curve, and so a power meter is connected at the output of the laser. A screen shows the actual power value, which is captured in one of the interfaces by means of the USB port. The model that has been used for the experiments is the Newport 842PE, which can measure optical power over a wide wavelength range.
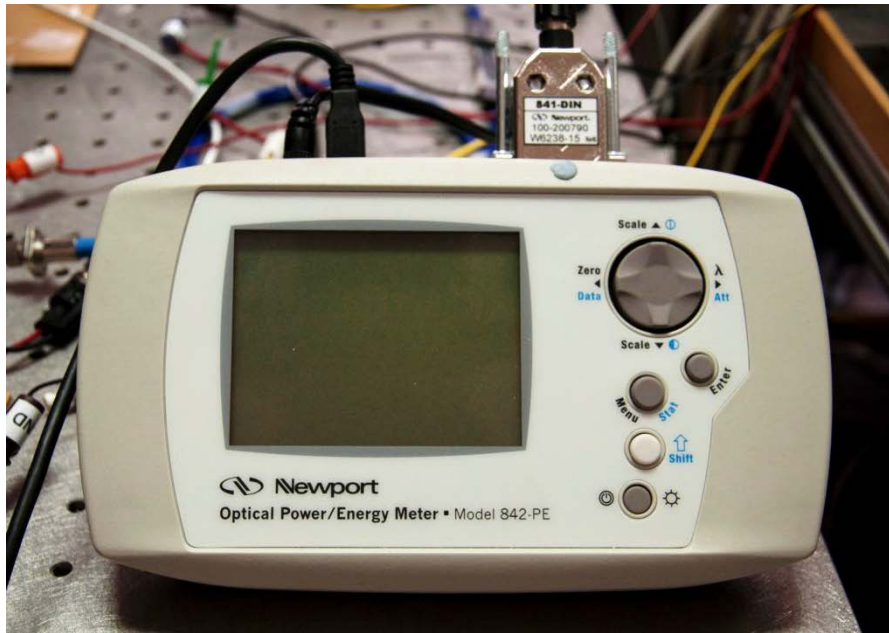
Figure 21. Newport 842 PE Power Meter

2.1.2. Detailed description

The chosen programming language for this tool was LabView, a product of National Instruments, due to their extended presence in instrumentation environments and its versatility. A general view of the graphic user interface (GUI) can be seen in Figure 22
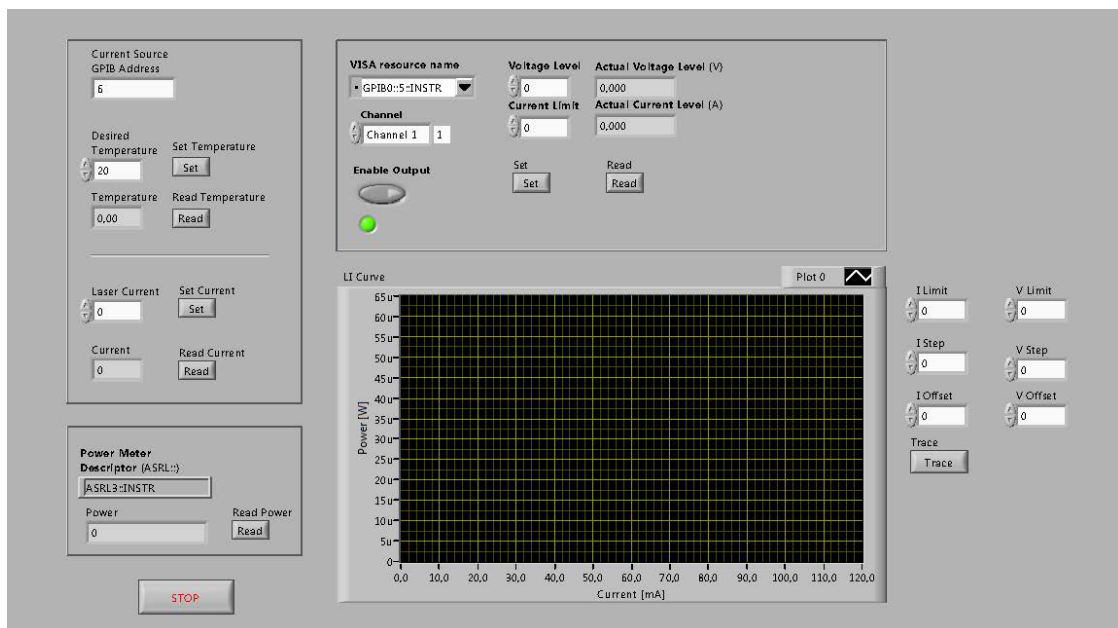
Figure 22. PI characterization tool's front panel

The interface is divided in four clear sections: Diode controller, Voltage source, Power meter and PI curve control. Each one is described in detail in this section.

2.1.2.1.   Diode controller

As it was mentioned earlier, the diode controller is managed by the GPIB bus. The direction is assigned directly in the instrument and it must be configured in the

instrumentation interface for it to work adequately. In this case, the primary direction of the instrument in the laboratory is number 6.
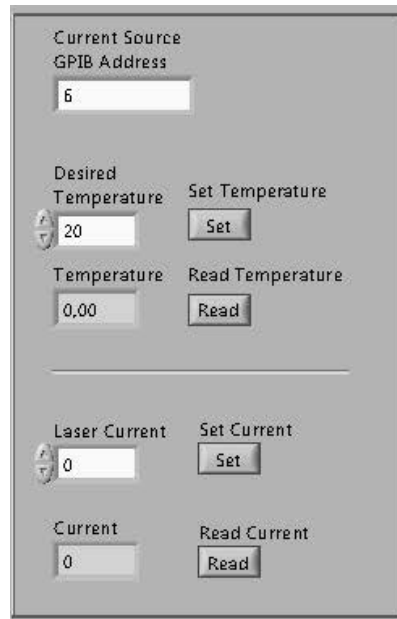
Figure 23. Diode controller section

Once connected, the user has access to some basic actions which are necessary for the purpose measurements. In first place, the temperature of the measured lasers can be set in the field 'Desired Temperature' seen in Figure 23. By pressing the 'Set Temperature' button, the diode controller will set the laser's temperature to the chosen one.

Users must be extremely careful with this choice. If the selected temperature is too low for the measuring environment, the laser can condense some of the water present in the air, damaging the devices in the worst case possible. For the present project, the temperature was varied between 16 and 18 Celsius degrees, because below these values, it was observed water condensation. Another function was added to check the real temperature at which the device is. By pressing the 'Read Temperature' button, the real-time value is presented in the field at its side.

The second main characteristic of the diode controller is the possibility of injecting a continuous current into the device through the corresponding probes of the station. The same functions that have been developed for the temperature have also been implemented in this stage, by means of the corresponding 'Set Current' and 'Read Current' buttons.
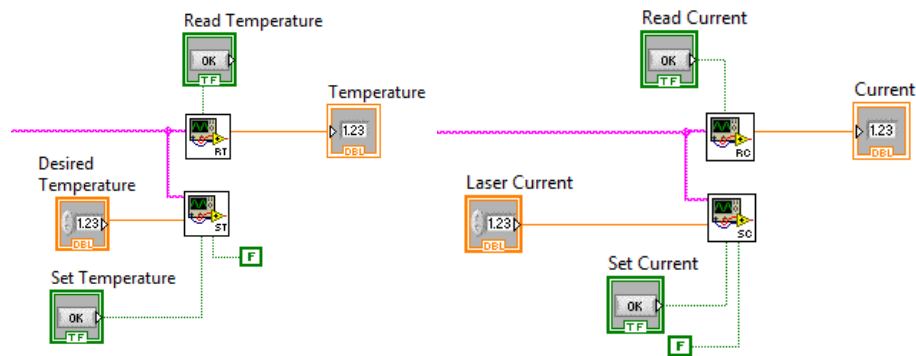
Figure 24. Fragments of diode controller's section programming

Figure 24 shows two fragments of the programming of the instrumentation tool. In them, it can be identified the toggle buttons (green border), numeric fields (orange border) and four subVIs that have been developed to control the Read and Set functions for temperature and current.

2.1.2.2. Voltage source

As well as the diode controller, the voltage source is operated over the GPIB instrumentation bus. For various instruments to work together, they must have been previously configured with different GPIB directions. In this case, the HP voltage source's direction was set to 5.
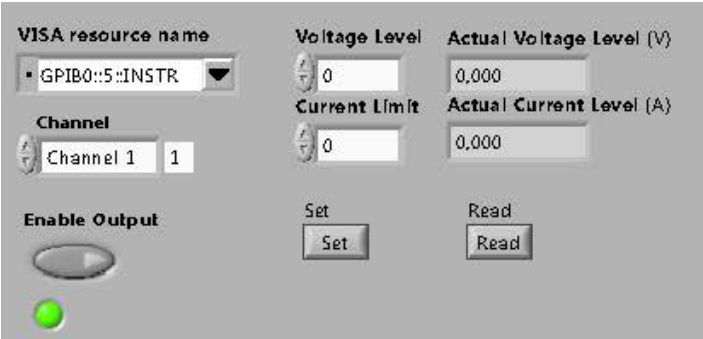
Figure 25. Voltage source section

The manufacturer of this instrument provides the users with some help to program. Instrument's drivers were supplied with the current LabView distribution (National Instruments LabView 2010), so the control is easier.

In this case, the controls include a voltage level and a current limit for each of the three channels of the voltage source. Additionally, a toggle button was included to control the activation of the output.
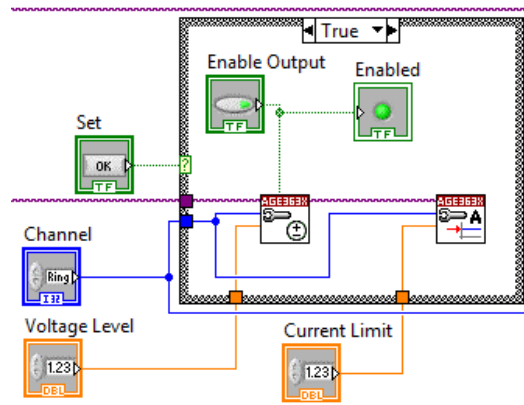
Figure 26. Fragment of voltage source's section programming

Figure 26 shows a fragment of the program, including the provided instrument's drivers, which are the white boxes with their upper part in red.

2.1.2.3.   Power meter

This is the simplest section of the whole GUI. However, the power meter does not use the same bus as the two previous instruments. The Newport device is operated through a serial connection, and it must also be configured at the beginning. An RS232 (Recommended Standard 232) to USB (Universal Serial Bus) converter is used, so it can be easily plugged into any computer. The operating system (OS) assigns a direction to the serial port and it must be consulted to configure adequately the direction of the instrument in the interface.

As it can be seen in Figure 27, the 'Read Power' button will print the instant measured value of the power meter in the corresponding field.
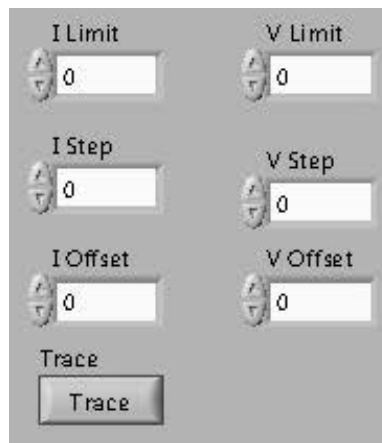
Figure 27. Power meter section

2.1.2.4.   PI curve control

The main objective of this instrumentation tool was to measure de PI curves of laser devices. After explaining the control of each laboratory instrument separately, this section is intended to unify them to make automatic measurements without any more interaction of the user.

There are six parameters to be configured (Figure 28). On one hand, the voltage control is divided in three fields. A PI curve is traced for each value of voltage corresponding to the sequence $V_{SA} = \{V_{offset}; V_{offset} + V_{step}; V_{offset} + 2V_{step}; \dots; V_{limit}\}$. Beginning from the offset value, the voltage is increased the step quantity for each trace until the limit is reached. On the other hand, the current is swept completely in each trace in the same way as the voltage.

Figure 28. PI curve parameters

In conclusion, the procedure is the following. In first place, the voltage is fixed to its offset value to begin with the first PI trace. The current is increased in the diode controller, measuring the optical output power at each point. When all the possible current values have been swept, the voltage is updated by increasing the step value and another PI curve is traced by sweeping the current again.

All the traces are automatically presented in the graphic of the GUI (Figure 29). Additionally, all the traces are stored automatically so they can be studied offline.
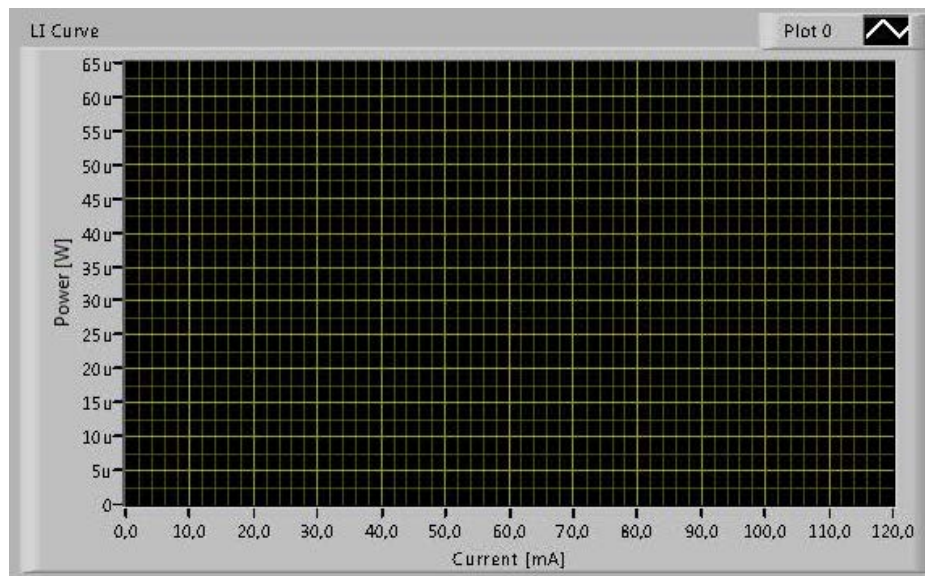
Figure 29. PI curve graphic

2.2. Phase Noise Characterization

Mode-locking ring lasers are pulsed at a certain repetition rate. In practice, this situation leads to a radio frequency spectrum that must be studied to characterize the devices of the project. Thanks to this spectrum, it can be assured that the lasers are pulsed, being in mode-locking regime. Later, another proof is presented by studying the pulse train emitted by the laser and received by an optical autocorrelator.

A spectral tone can be found at a determined frequency for a specified ring laser. When analysing the optical spectrum of the laser, the laser's modes are equally spaced at the repetition rate of the device. A photodetector allows the conversion of the optical signal into a radiofrequency one to be captured by the RFSA.

In case of having a ring laser working in the mode-locking region, the spectrum analyser can give information about the repetition rate of the pulse train and the noise components present in the signal. Noise components can be mainly classified into amplitude and phase terms [21].

2.2.1. Noise components

The two components of noise can be clearly distinguished in Figure 30. The maximum variation between a signal and its medium value is considered as the amplitude noise. The temporal displacement from its predetermined position is caused by the phase noise.
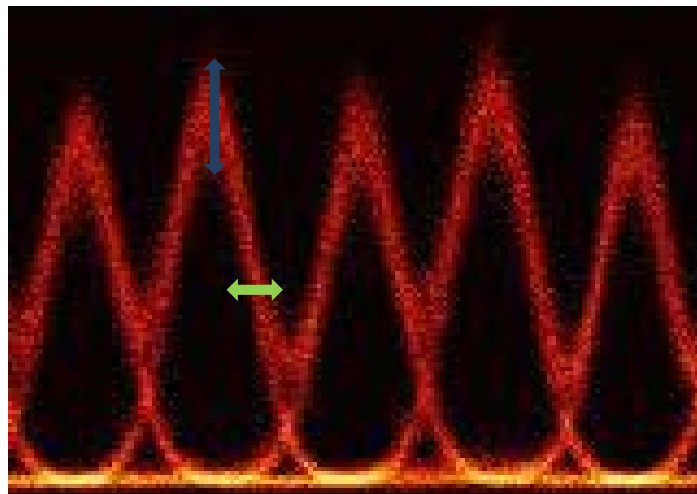
Figure 30. Amplitude noise (blue) and phase noise (green) in a data pulse eye

To evaluate the phase noise impacts adequately, it must be determined their importance for the transmission system in which they are present. For low frequencies up to a few megahertz, feedback networks and clock recovery can deal with phase noise. However, for higher frequencies, phase noise is critical in OTDM systems, as the clock recovery circuits do not have enough bandwidth to generate synchronization signals in these cases. A fast readjustment of the control pulses is then difficult [21].

2.2.1.1. Amplitude noise

The amplitude noise taken from the electric spectrum is obtained by the following equation:

$$N_A = \sqrt{\int_{f_1}^{f_2} RIN df}$$

where it is taken the square root of the Relative Intensity Noise (RIN) integral. RIN is the output power's instability of the laser. The integral's limits are f_1 and f_2, where f_1 corresponds to the lowest frequency allowed by the RFSA and f_2 half the laser's repetition rate.

2.2.1.2. Phase noise

There are different ways of characterizing the phase noise. For this project, a single side band (SSB) measurement has been made for the observed carrier in the RFSA [21]. It has been implemented in the noise characterization's interface developed for this project.

The SSB noise level is defined as $L(f_m)$ and it is the ratio between the carrier's power at its central frequency P_0 and the lateral band's power at an offset frequency f_m. The resulting equation is related to a bandwidth of 1 Hz:

$$L(f_m) = \frac{P_{SSB}(f_m)|_{1Hz}}{P_0}$$

The precision of this measurement is limited by the analyser's intrinsic phase noise. For this reason, the RFSA manufacturer provides the instrument's phase noise, limit for the minimum noise that can be measured.
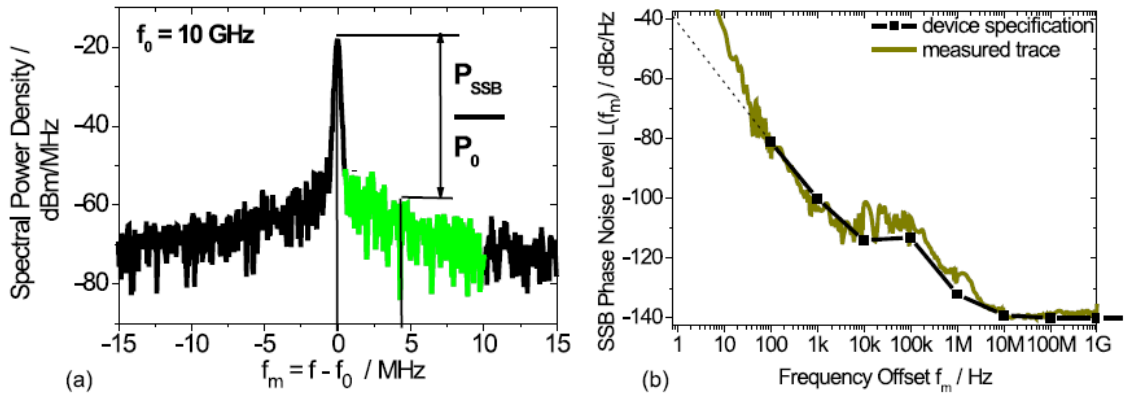
Figure 31. SSB Noise analysis (a) and device specification trace (b)

2.2.2. Instruments

This interface interacts with two instruments. To the already described diode controller, a radio frequency spectrum analyser is included.

2.2.2.1. Radio frequency spectrum analyser

Mode-Locking lasers have a comb spectrum, in which its modes are equispaced. Optical modes beating produce a radio signal of the same frequency as the modes' separation. So, to study this phenomenon, a radio frequency spectrum analyser is needed. The Optical-Electrical (OE) conversion is done with the U2t after amplifying the optical signal with 2 Erbium Doped Fibre Amplifiers (EDFAs).

All the parameters of the RFSA are controlled through the GPIB port, as well as the retrieval of the spectrum data. The instrument available at the laboratory was the Anritsu MS2668C.

Figure 32. Radio Frequency Spectrum Analyser

2.2.3. Detailed description

The objective of this interface is to control the laboratory's radio frequency spectrum analyser to automate the phase noise measurements necessary for the ring laser devices. A general view of the interface is presented in Figure 33.
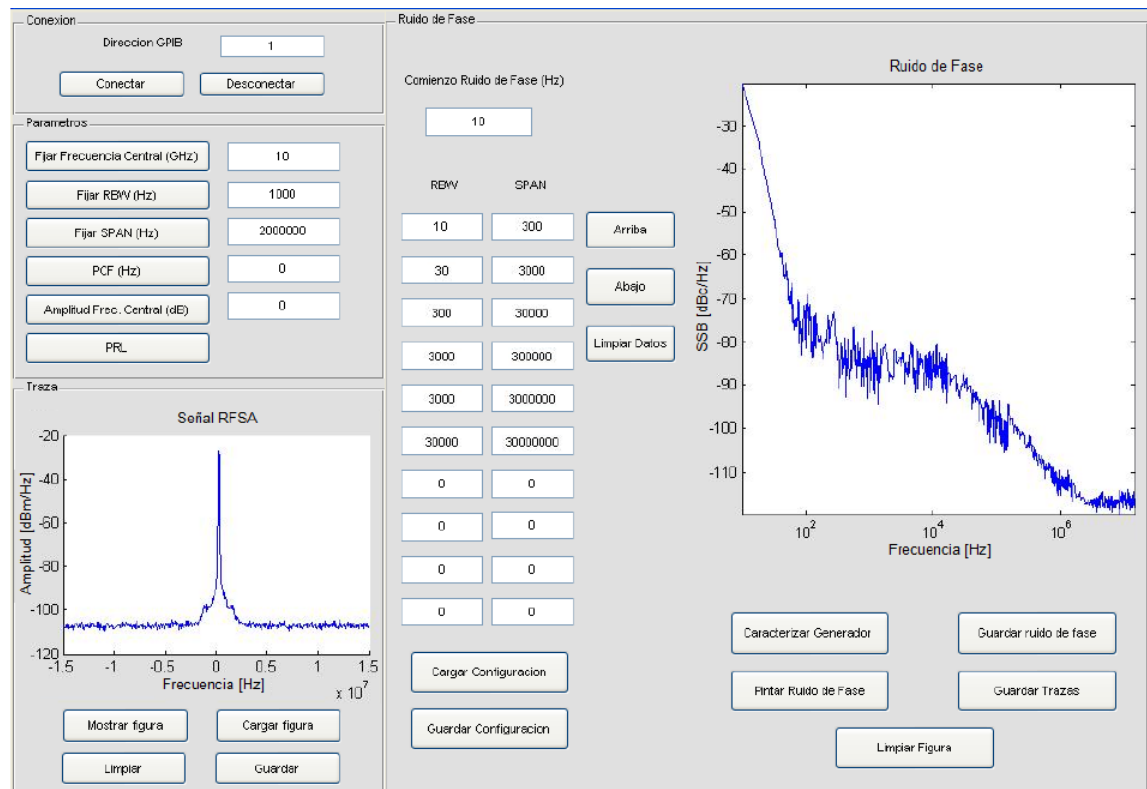
Figure 33. General view of the noise measurement interface

For this interface, a different language has been employed, being MATLAB the choice due to the absence of LabView drivers for the Anritsu MS2668C, which is the instrument of which the laboratory disposes.

The interface is divided in four different regions: instrument connection, parameter definition, trace visualization and phase noise measurement. These regions are explained in detail.

2.2.3.1. Connection

This panel allows the connection between the measurement interface and the spectrum analyser. The connection is made by the previously mentioned GPIB instrumentation bus, as well as other instruments of the laboratory. For this particular case, the assigned direction was number 1, which has to be different to any other instrument's direction. By default, it is the chosen direction which appears in the connection panel.

Obviously, the user is in charge of checking that the direction is the adequate for a correct operation of the interface. The connection is the first action to be made, and the interface will notify the user to connect the instrument before making any other operation.

Figure 34. Connection panel

2.2.3.2.   Parameter control

For a correct measurement, some parameters of the radio frequency spectrum analyser must be configured. In Figure 35 it can be seen that these parameters are the central frequency, resolution bandwidth (RBW) and span, which are the first three fields.

By means of the central frequency and the span, it can be defined the set of frequencies in which the spectrum measurements are made. For example, taking a central frequency of 9 GHz and a span of 2 MHz, the measured frequencies will be $\omega \in \{9\,GHz - 1\,MHz,\ 9\,GHz + 1\,MHz\}$. In conclusion, the span is the measurement bandwidth in which the spectrum will be measured around the central frequency.

The resolution bandwidth establishes the capacity of a spectrum analyser to distinguish between two near frequency components. The analyser offers different IF (intermediate frequency) filters with different bandwidth. This choice is crucial for the measurement, as it also affects the sensitivity of the instrument. When the measurement bandwidth of the filter is reduced, the quantity of thermal noise that is integrated decreases. As a consequence, the output signal is less noisy, improving the sensitivity value.

Whenever one of these three buttons is pressed, the value is sent to the RFSA and a new trace is plotted in the instrument to visualize the changes.

Figure 35. Parameter control panel

The importance of selecting adequately the resolution bandwidth with respect to the span arises when the sweep time is taken into account. The sweep time is the total time that the analyser employs to sweep the entire frequency margin defined by the span. This time changes dramatically with the choice of the resolution bandwidth. For a big span value combined with a low resolution bandwidth, the measurement can take several hours.

The next three buttons implement useful functions. In first place, PCF means 'Peak to Centre Frequency' and it adjusts the maximum measured power to the central frequency of the measurement. When the centre frequency is updated, it appears in red colour in the corresponding field. It is extremely useful to centre a peak that is not correctly aligned to measure it.

Secondly, the central frequency amplitude button measures the peak power level of the processed signal, being updated in red in the nearby field. In last place, the function PRL 'Peak to Reference Level' has been implemented. When pressed, the signal's maximum power level is assigned to the instrument's reference level. Immediately afterwards, a new sweep is made to show the new location of the trace.

2.2.3.3.   Trace visualization

This panel offers the possibility of visualizing the analyser's trace. When the button 'Mostrar figura' is pressed, the instantaneous value of the trace is presented in the graphic of the panel. For this RFSA, it is composed of 501 equispaced points, which are retrieved automatically by the GUI. The necessary parameters include the format of the received data, and they are already implemented for a transparent usage for the user.

An extremely useful function of this panel is the saving option. By pressing the button 'Guardar' a window will pop up so the user can select a path and name for the generated Matlab file with .mat extension. The frequency and amplitude values are stored in this file for their further use. Additionally, the saved figures can be loaded into the graphic area by clicking the 'Cargar Figura' button and selecting the adequate Matlab file.

Images are kept in the graphic area, allowing the user to superpose another one over the measurements that have already been made. To work on a blank area, users must push the button 'Limpiar' to erase the previous traces.
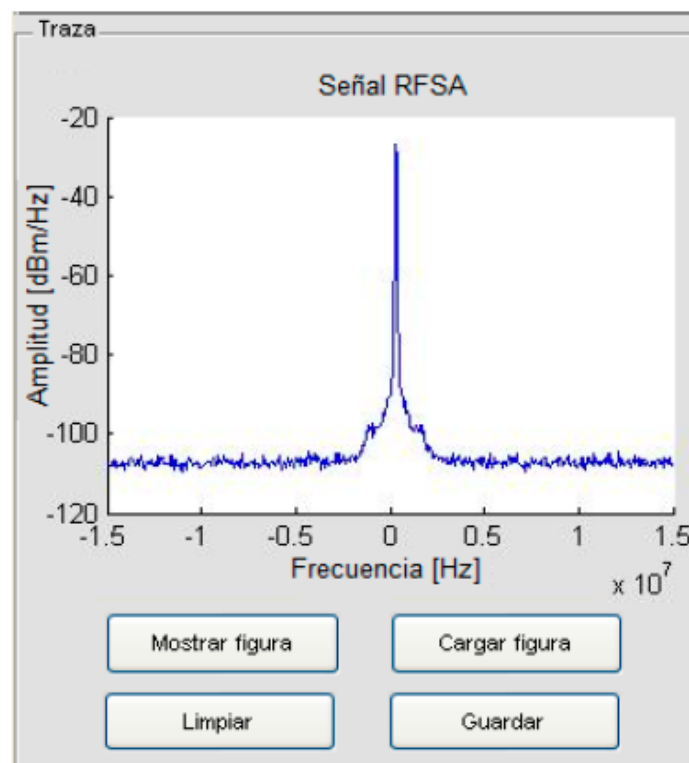
Figure 36. Trace visualization panel

2.2.3.4.   Phase noise measurement

The phase noise measurement is made in several sweeps over increasing values for resolution bandwidth and span. For frequencies close to the carrier, the resolution bandwidth

is kept in small values and swept over small spans of frequency. In this way, the measurements are made with a good accuracy and are not costly in time. The methodology of the measurements is detailed in the following paragraph.

For each sweep the corresponding configured values are used. If the trace is the first one, the initial point to consider is the frequency in which the peak power is present. From that point until the end, all the values are stored. When the second and following traces are measured, the initial value stored corresponds to the last frequency measured in the previous sweep, taking again all the values from that point until the end of the measured span. All that values are then normalized with respect to the carrier's maximum value and a resolution bandwidth of 1 Hz, with the resulting units of $dBc/_{Hz}$

The values are stored in two axes, corresponding to the frequency and amplitude values of the phase noise. The values obtained for the graphic in Figure 37 correspond to the characterization made to the radio frequency generator present in the laboratory, which fit with the data provided by the manufacturer.

Figure 37. Phase noise measurement panel

For this particular case, the characterization is made through 6 different RBW-SPAN pairs, which must be configured in the fields which are provided at the left of the panel. The

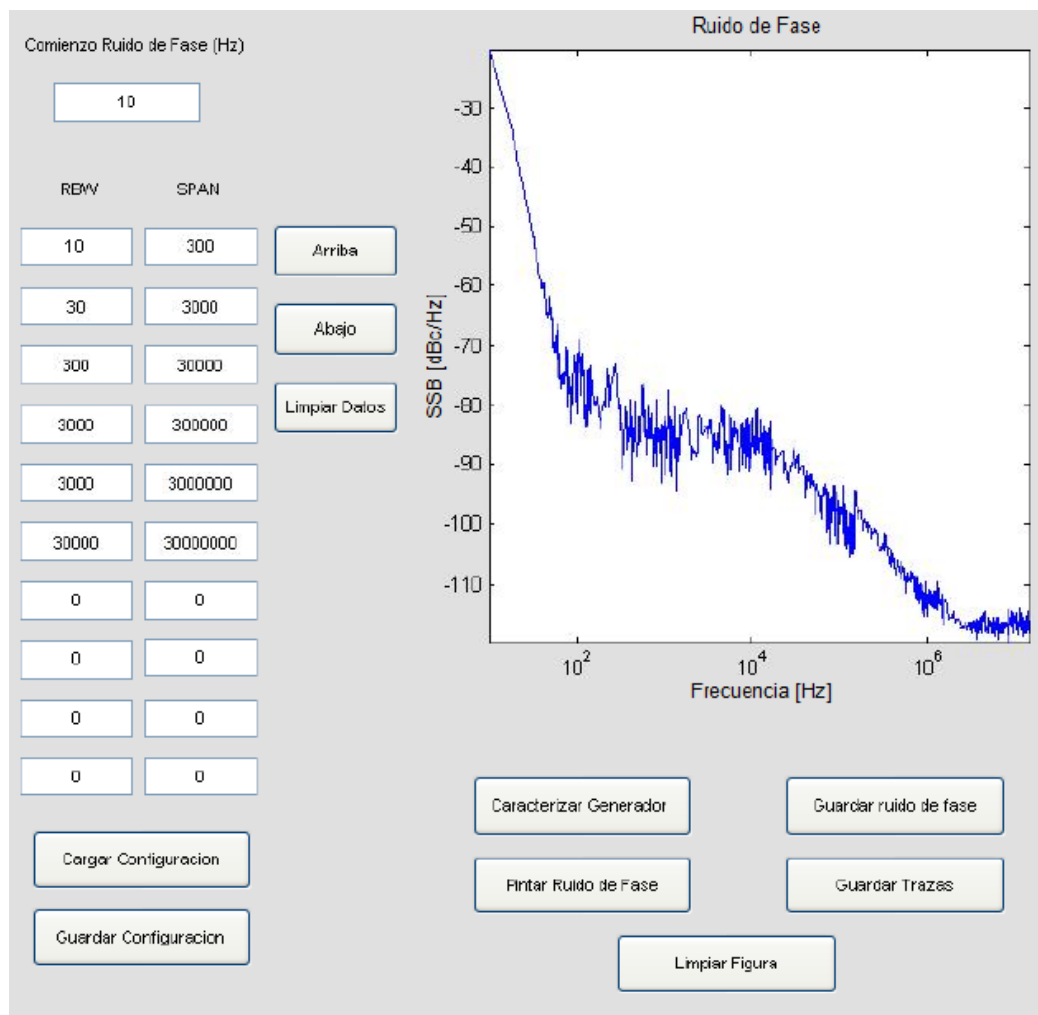initial value of the field 'Comienzo Ruido de Fase' (Phase Noise Start Point) is set to eliminate some oscillations in the peak value of the carrier. In the generator case, it is set to 10 Hz due to the stability of the signal, but for lasers it is usually configured as a larger value as the values are not so stable.

Buttons 'Arriba', 'Abajo' and 'Limpiar' (Up, Down and Clean) allow the user to interact easily with the RBW and SPAN values. New measurement intervals can be defined or removed without reconfiguring all the fields, as well as offering the possibility of erasing all of them. Additionally, the buttons 'Cargar configuración' and 'Guardar configuración' (Load and Save configuration) allow to store any configuration defined by the user in a Matlab file and then load it again in another occasion.

When all the values have been configured, the user must press the button 'Pintar'. The values are taken from the left-hand fields, but the configured RBW values may not be permitted by the RFSA, as they must coincide with the resolution bandwidth filters offered by the instrument. In case the configured values are not correct, the values are approximated to the nearest filter value and then updated in the corresponding field in red colour so the user can notice it.

Once the noise figure has been measured completely, the user can access to two more functions. The generated single side-band noise trace can be saved by pressing the button 'Guardar ruido de fase', and a Matlab file is generated with the axes of the figure. Another option is to save the complete traces that have been taken during the measurement without being processed. To broaden the possibilities of this interface and the following treatment of the radio frequency spectrum traces, they can be stored in two ways. In first place, a Matlab file can be created for each trace, in which the trace will be stored together with the RBW, SPAN, central frequency and frequency axis. Each file will be named with a string chosen by the user and the RBW and SPAN parameters, i.e., name_RBW10_SPAN5000.mat. If the user chooses to save the traces in Excel format, a new sheet will be used for each trace instead of creating a new file.

As well as in the previous panel, a button 'Limpiar figura' allows the user to wipe out the existing traces so that new measurements do not overlap.

2.3.   Pulse autocorrelation

As it was described in the theory chapter, the mode-locking regime can be characterized by means of the pulse autocorrelation of the laser. Once the P-I-V curves and the phase noise have been obtained, the mode-locking can be corroborated by the study of the pulses emitted by the measured device.

2.3.1. Instruments

To check if the laser is working in multi-mode regime, an optical spectrum analyser can be used. In this way, by using a 90/10 coupler, a slight quantity of energy was visualized in the OSA while the rest of the light was amplified and directed to the pulse autocorrelator present at the laboratory. It was employed together with a new graphic user interface to characterize the pulses emitted by the ring lasers of the project.

2.3.1.1.   Optical spectrum analyser

The Optical Spectrum Analyser (OSA) offers a colour display in which the laser spectrum can be visualized. Different functioning modes have been distinguished for the studied lasers, as well as visualizing optical spectrum changes for changes in the injected current.

The communication with the Yokogawa AQ6370B was made by the given Yokogawa's interface, which works over an Ethernet connection. Data was collected graphically and in Excel files to treat it offline.

Figure 38. Yokogawa AQ6370B Optical Spectrum Analyser

2.3.1.2.   Autocorrelator

Due to the narrowness of this light pulses, a pulse autocorrelator must be employed to take measurements. At the input of the autocorrelator, the light beam is split: one of the arms of the internal interferometer is fixed, while the other one changes its length to sweep over a period of the order of picoseconds. Therefore, the total output is the multiplication of one of the pulses by a time-displaced copy of itself, being this result the autocorrelation of the pulse.

Thanks to one of the developed interfaces, the resulting autocorrelation can be downloaded to a computer, where it can be treated. The most important function is the one that allows fitting the measured autocorrelation to the three most common models (Gaussian,

Sech^2 and Lorentzian) and make an approximation of the pulses Full-Width Half Maximum (FWHM).

The instrument, an APE PulseCheck Autocorrelator, consists of two modules. The first one is the interferometer (Figure 39) and the second module is in charge of processing the autocorrelation signal at the interferometer's photodetector (Figure 40). It is managed by an USB connection.
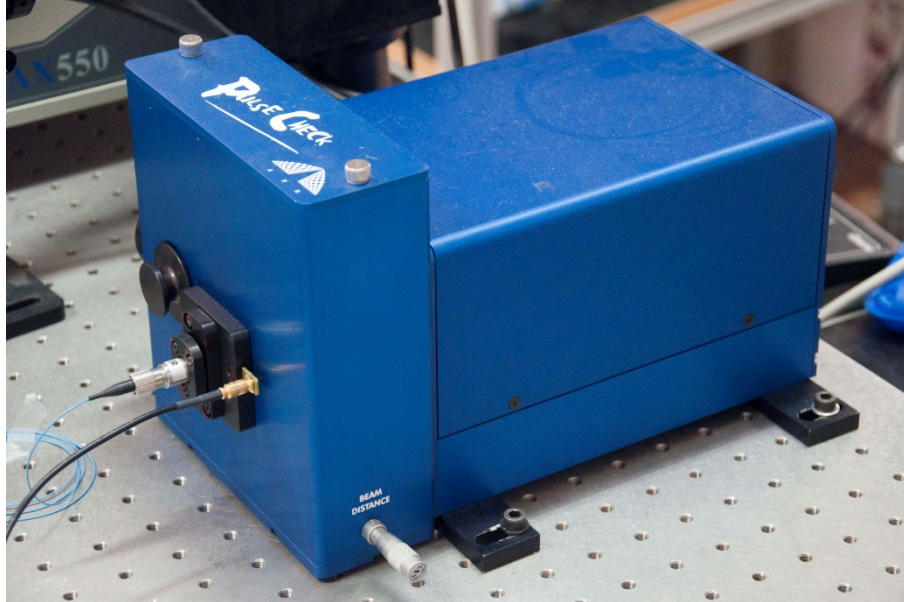
Figure 39. Interferometer module of the APE Photonics Autocorrelator
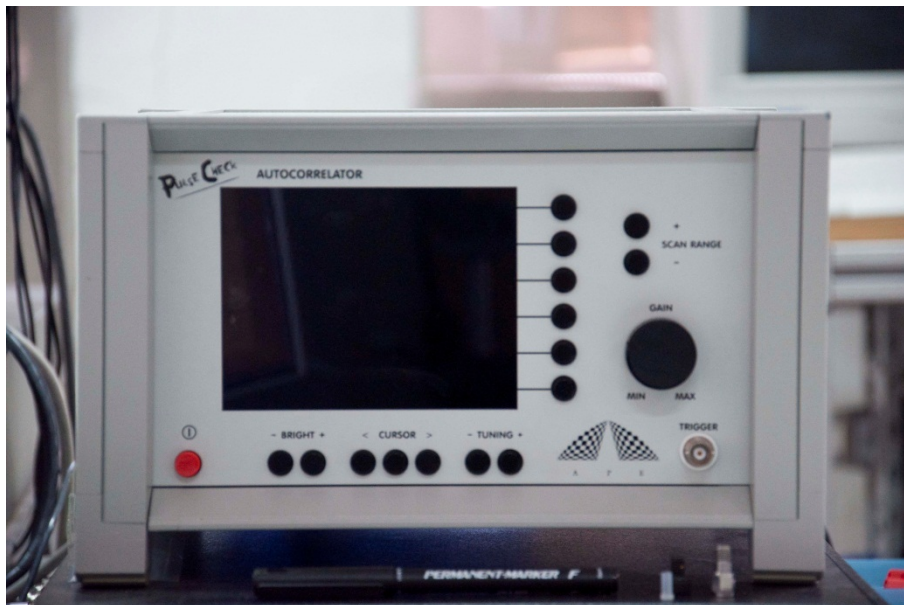
Figure 40. Control module of the APE Photonics Autocorrelator

2.3.2. Detailed description

This interface has been programmed with Matlab, as well as the first P-I-V characterization tool. With the help of this interface, the autocorrelator's signal can be processed, obtaining extremely important parameters as the pulse width. It is composed of

four different panels: connection, control, pulse visualization and pulse fit. A general image of the interface is presented in Figure 41.
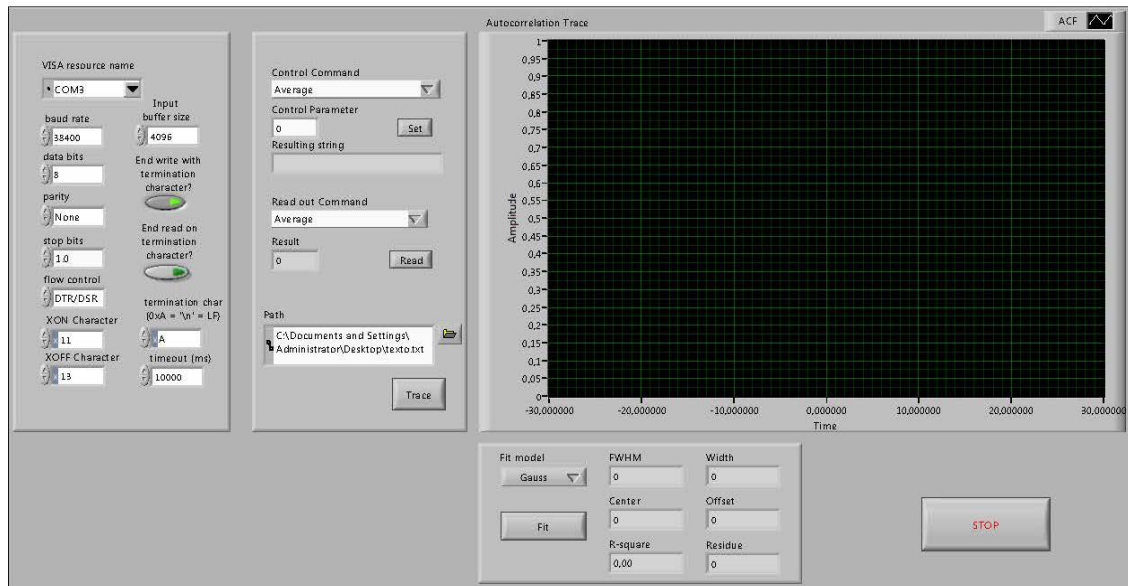
Figure 41. Pulse autocorrelation interface

2.3.2.1. Connection

The autocorrelator is connected through a USB serial connection. The operative system will assign a serial port number to the USB port to which it is connected, and the user is in charge of configuring it in the field VISA resource name (see Figure 42). The rest of the configuration parameters present in this panel are dependent of the autocorrelator, so they are defined by the instrument's manufacturer in its technical datasheet. By default, these parameters have been set to meet the necessary values to work with the autocorrelator of the laboratory.
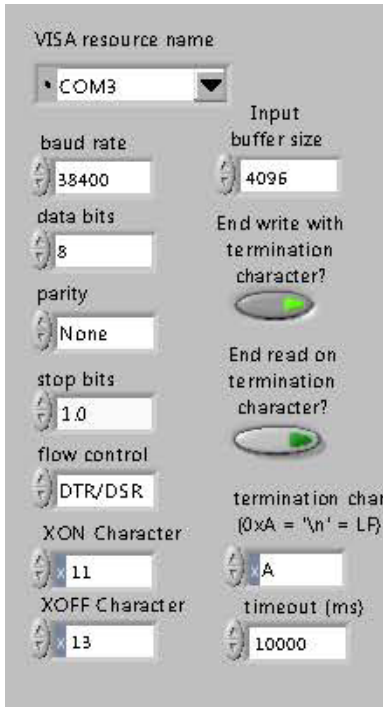
Figure 42. Connection panel

2.3.2.2. Control

The graphic user interface implements all of the possible functions defined by the manufacturer for the autocorrelator through a remote connection. By means of the pop-up list 'Control Command', the user can select the desired option and then write the corresponding value in the field 'Control parameter'. When the 'Set' button is pressed, the command is written to the autocorrelator. For a correct operation, the resulting string is displayed in the field beneath, while this same field will show an error if the input parameter must be revised, indicating the possible values that the user can introduce for a specific option.
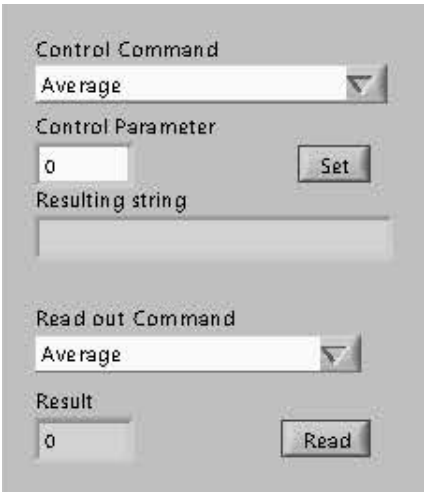
Figure 43. Control panel

As it is showed in Figure 43, the second function implies reading a series of parameters that are already configured in the autocorrelator. The user must select an option from the list

'Read out Command' and press the 'Read' button. The read value will be displayed in the field 'Result'.

2.3.2.3.   Pulse visualization

This panel is split in two differentiated parts. In the first one, the user can choose the path and file in which a measurement will be saved. It is important to note that each measurement must be stored in a different file or the information will be overwritten.

When the user presses the button 'Trace', the autocorrelation trace is presented in the graphic area, normalizing its value to one. The pulse information, together with the time axis and the autocorrelator's configuration parameters are then automatically written to the selected file.
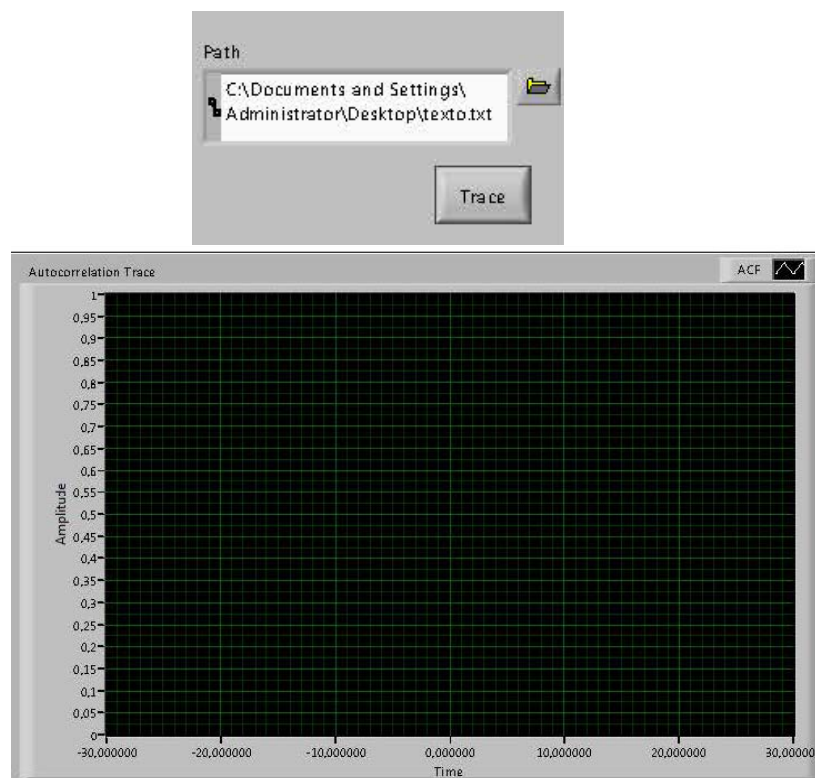

Figure 44. Pulse visualization panel

2.3.2.4.   Fit

The fit panel implements one of the most important functions of this interface. As it was explained in the first chapter, there are a series of lineshapes under study for autocorrelation traces. Three different shapes are considered to be the most important ones: Gaussian, Lorentzian and Sech^2 (Table 2). Hence, when a pulse autocorrelation has been measured, these three different fit models can be adjusted to the trace. Simply by setting the chosen model and pressing the 'Fit' button, the six parameters of the right side are updated with the values corresponding to the new approximation.

The FWHM field corresponds to the Full Width Half Medium of the <u>temporal</u> pulse, and must not be confused with the autocorrelation's width. Additionally, the R-square field gives a percentage of the goodness of the fit.
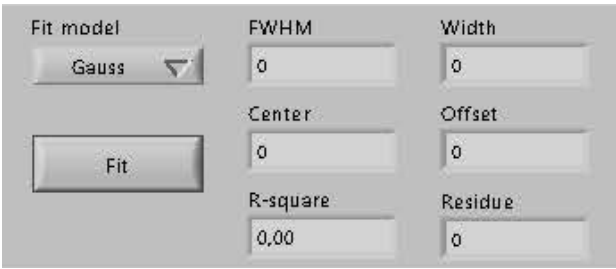
Figure 45. Fit panel

2.3.3. Fit tool

Not all measures are made online, so another similar tool was developed in parallel to this interface. The fit tool allows loading a measured autocorrelation trace and making the fit offline. A general view of the front panel is showed in Figure 46.

Figure 46. Fit tool

Chapter 3

Obtained results

The above described interfaces were employed to obtain data from the series of rings presented in the first chapter. Although both asymmetric and symmetric lasers were measured, the most important results have come from one of the symmetric ones. The chip's lasers are numbered from 1 to 8 as they are disposed in the chip, being number one the upper device and number 8 the lower device. Laser number 6 presents optimum results, so these ones are boarded in this section.
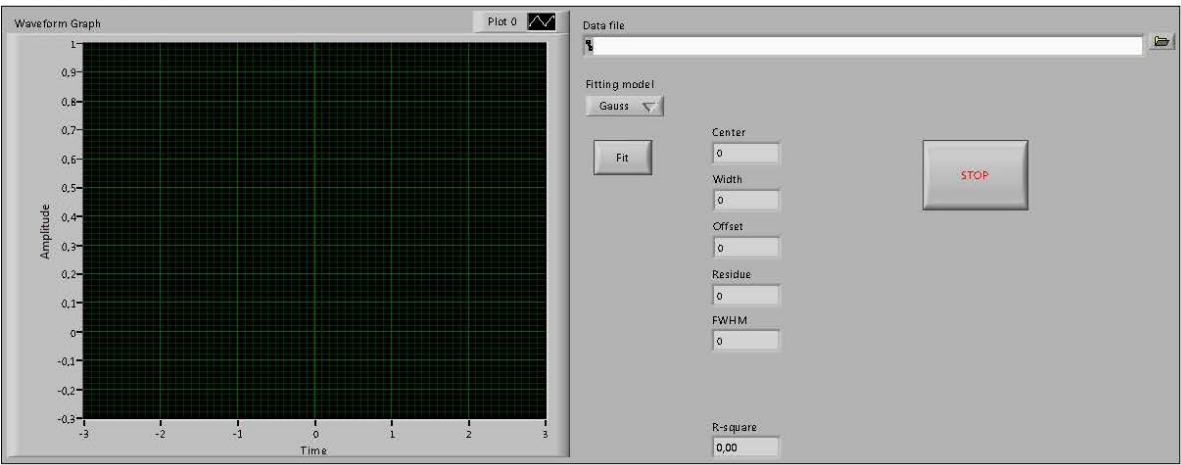
The methodology that has been followed implies four different measures. In first place, P-I curves were taken for both sides of the laser to study the CW and CCW propagating modes, allowing to determine their performance and establishing the threshold current. Next, the optical spectrum was taken for different voltages in the saturable absorber by means of the instrument's proprietary software, following a radio frequency tone characterization. Once these measurements were made, the emitted pulses were studied to determine the mode-locking operation of the device.

3.1. Symmetric Ring Laser

This section collects the results obtained from a symmetric ring laser, specifically ring number 6. The device has to gain sections separated by a saturable absorber, which were connected as shown on Figure 47. The two independent gain sections were biased using two independent current sources, one which could only be fixed manually while the other was controlled with our interface, allowing us to program current sweeps automatically. The saturable absorber section was reverse biased by means of the HP voltage source.

It is noticeable that the CW and CCW output waveguides are tilted 7 degrees to avoid reflections back into the ring from the fibre that collects the output light. The cavity length was

designed for a repetition rate of 15 GHz, defined by the active-passive cavity, and a saturable absorber length of 3 µm.
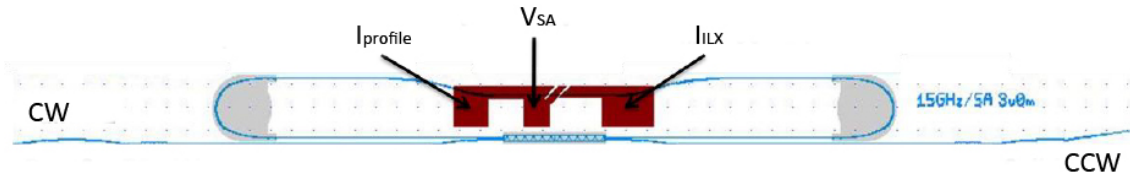

Figure 47. Ring laser 6 connection diagram

3.1.1. P-I-V Curves

3.1.1.1. Setup

The first step to study any laser device is to obtain the dependence of the optical output power on the applied bias current, known as P-I or L-I curve. The left current probe, named $I_{profile}$, was driven by a current source which was fixed at 60 mA, while the right current probe was swept from 0 to 60 mA in steps of 2 mA.

Since in addition to the gain regions, our device presents a saturable absorber, this curve has been obtained at different reverse bias points, determining the range of the different operating regimes in the device. The different voltages applied to the saturable absorber range from 0 to 3 volts in steps of 0.5 V.

The ring laser actually has two light outputs, one for each propagation direction (CW and CCW). Two optical fibres with AR coating were placed at either sides of the laser chip optimizing the coupling. Immediately after the output fibre, an isolator was connected before reaching the power meter as a prevention method to avoid completely back-reflections. After a first alignment of the two outputs, the curves were measured with the P-I-V characterization tool and the data stored in measurement files.

3.1.1.2. Results

In the following figures, the relevant P-I curves are presented. In each case, the two traces that appear correspond to the CW and CCW output powers, which allow observing the exchange of power between directions.

When the saturable absorber is biased at 0 V, shown on Figure 48, three different regions can be appreciated in the plot. Up to 10 mA, the laser has not reached the threshold current, so there is only the spontaneous emission at the outputs. Between 10 and 22 mA, the CW and CCW modes begin with the stimulated emission, and from 22 to 60 mA, the CCW mode dominates the emission.

As the voltage in the saturable absorber is increased, this section modifies the competition between the modes and noticeable changes appear. When the reverse voltage in the saturable absorber is increased slightly (-0.5 V) we observe the mode competition from the threshold level up to 30 mA. At this level, the two modes are stabilized until 60 mA as shown on Figure 49.

Further decrease in the absorber section voltage shows how the optical power is mainly taken by the CCW mode, from threshold current up to 26 mA. At this current level, we observe the power on the CCW direction reaching its maximum. An increase in the current switches the optical power into the CW mode, which rises in an unstable way. It must be said that the second fibre's support is not as good as the first one, and the instabilities may be caused by this reason.

The evolutions of the optical power traces are similar to those previously observed on ring lasers, and so the results were expected instead of a straight lasing curve.
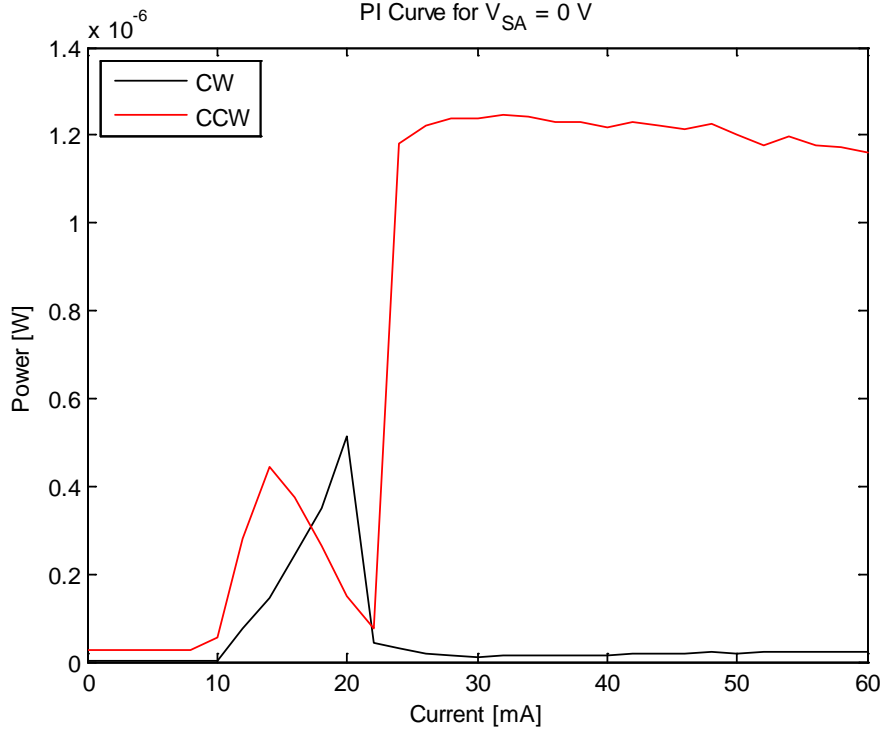
Figure 48. PI curve for V_{SA} = 0 V
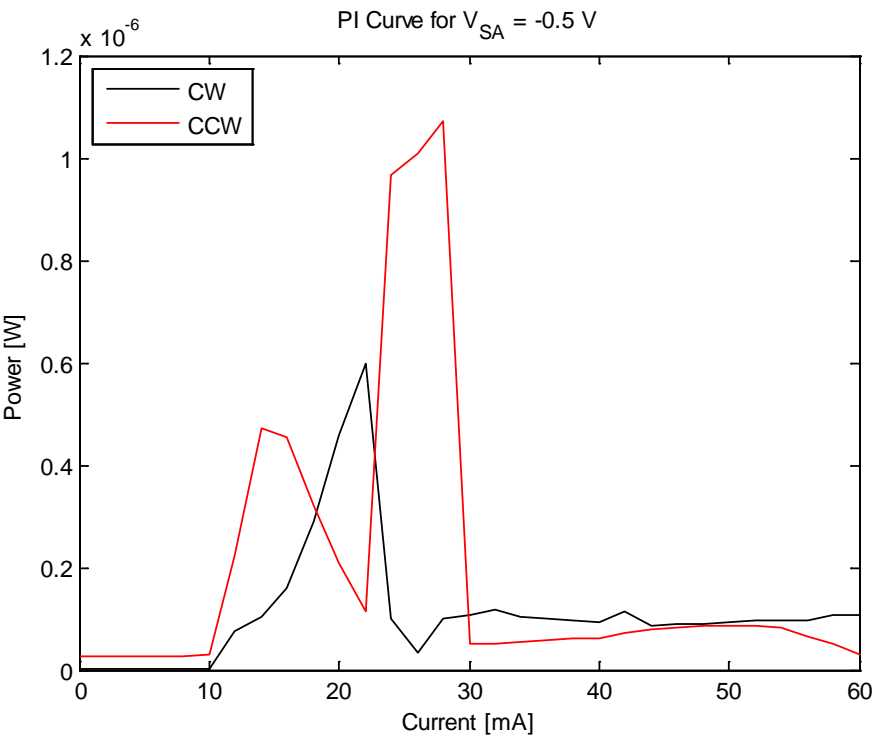
Figure 49. PI curve for V$_{SA}$ = -0.5 V
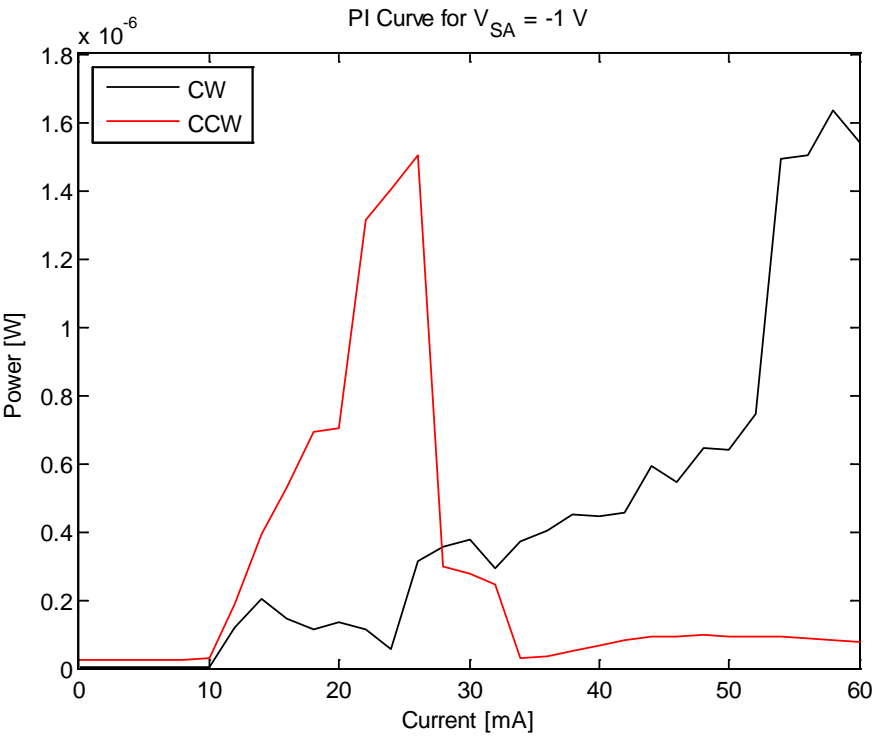
Figure 50. PI curve for V$_{SA}$ = -1 V
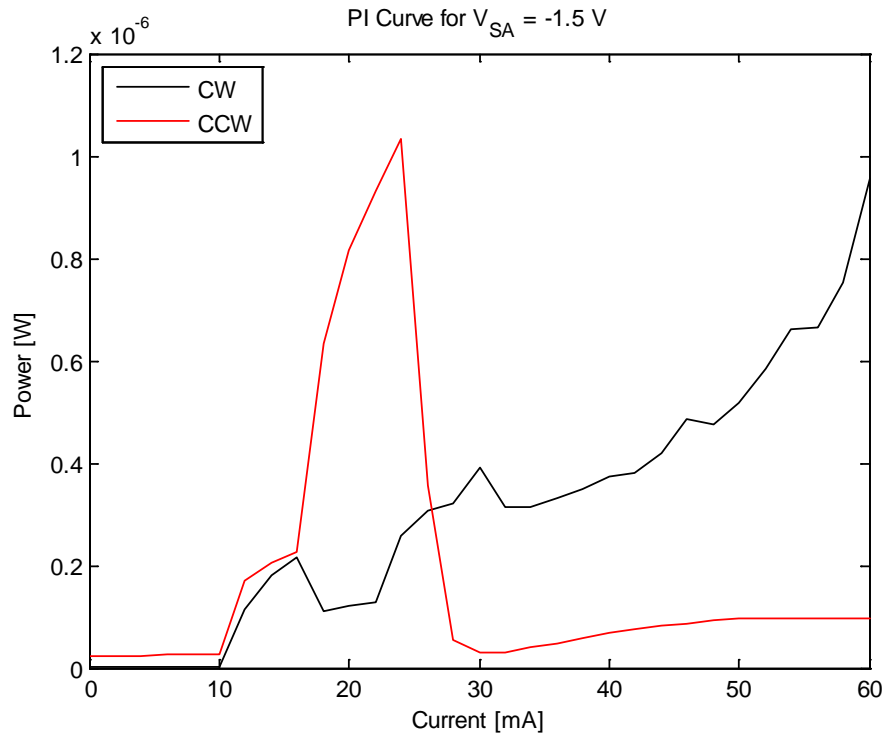
Figure 51. PI curve for V_{SA} = -1.5 V
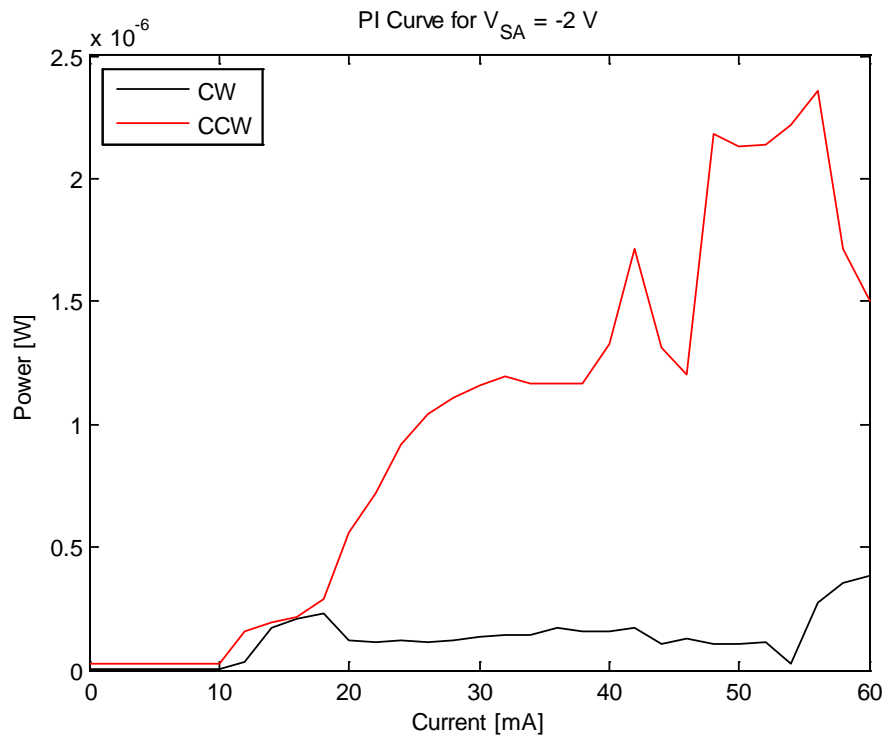
Figure 52. PI curve for V_{SA} = -2 V

The curves in Figure 51 are very similar to the ones seen in Figure 50, but a slight difference must be underlined. The peak of maximum power for the CCW mode is now shifted to a current of 24 mA, following the trend of the graphics with voltages of -0.5 V and -1 V.

From the reverse voltage of -2 V, the two traces exhibit a steady increase, without switch between the CW and CCW modes (Figure 52, Figure 53 and Figure 54). However, much less light is collected at the CW output, a result very similar to the one reported by Tahvili [27]. This leads us to suspect with the possibility of a mode-locking regime for the bias parameters where we find stable steady increase of power in the P-I traces. Further characterization is needed to confirm this hypothesis, based on the observation of the optical and radio frequency spectra as well as the autocorrelation.

Finally, Figure 53 and Figure 54 are very similar. The threshold current moves to larger values due to the generated losses of the polarized saturable absorber.
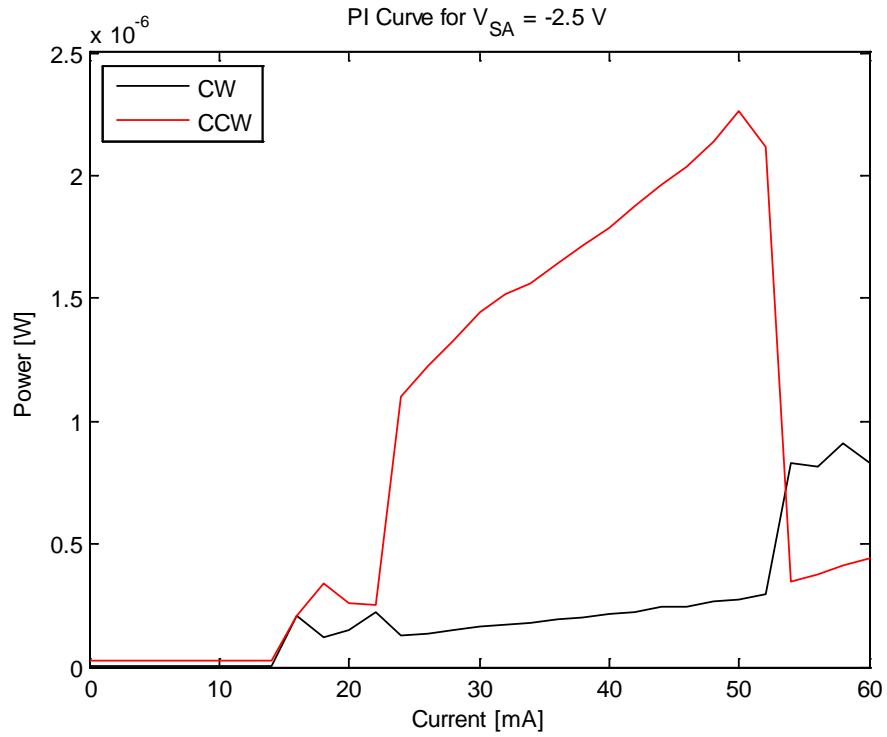
Figure 53. PI curve for V_{SA} = -2.5 V
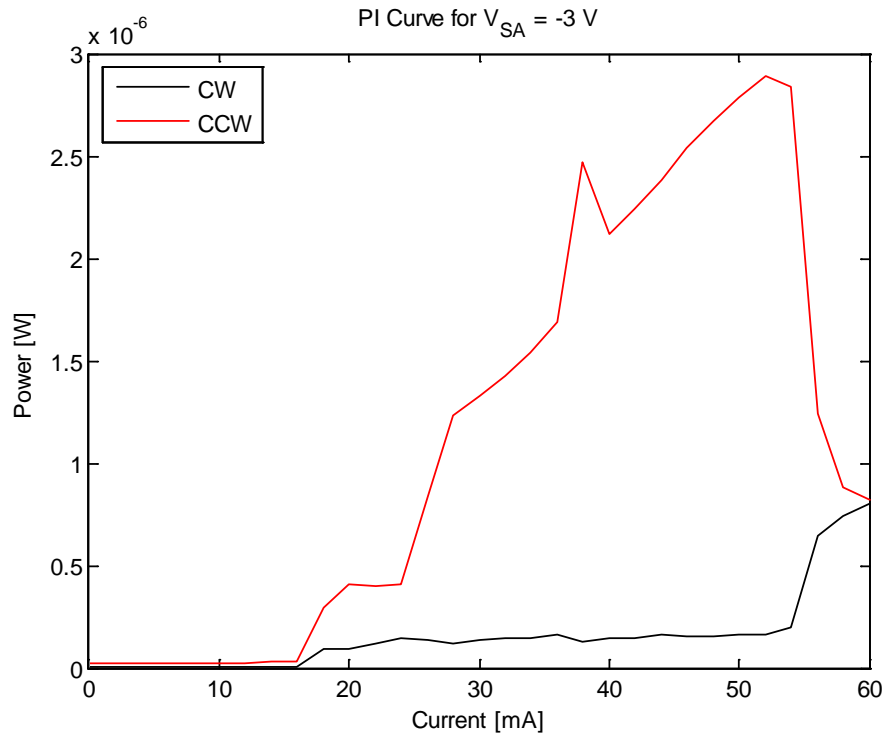
Figure 54. PI curve for V_{SA} = -3 V

3.1.2. Optical spectrum

A further step in the characterization of the laser devices is to observe the optical spectrum. The optical spectrum reveals many details of the resonator, as the spacing among the peaks show points where light finds reflecting surfaces. In the ring laser resonator, the spacing among the main modes reveals the resonator length. In addition, the shape of the spectrum can also indicate the existence of a mode locked regime by its characteristic Gaussian shape. In that case, the distance between the modes is related to the repetition rate.

3.1.2.1. Setup

The setup is very similar to the P-I measurements, except for the fact that the light is taken to the Optical Spectrum Analyser. The resulting spectrum that we present corresponds to the bias conditions Iprofile = 60 mA and IILX = 50 mA.

We have selected this current combination since on Figure 52, Figure 53 and Figure 54 can be observed that this particular point shows the maximum power for the CCW mode. The measurements have been made for the CCW output due to its higher output power, which will allow studying better the characteristics of the emitted light.

3.1.2.2. Results

The different traces of the optical spectra correspond to different reverse bias voltages for a fixed current pair ($I_{profile}$ = 60 mA and I_{ILX} = 50 mA). The first two graphics, Figure 55 and Figure 56 , corresponding to the reverse voltages of 0 V and -0.5 V show a single mode emission spectra of the ring laser. Almost all of the power is concentrated in one dominant mode, located at approximately 1570 nm.

However, as the reverse bias voltage decreases, it can be appreciated that some more modes appear at both sides of the main emission mode as it is evident in Figure 57 and Figure 58 with corresponding voltages of -1 V and -1.5 V. A zoom of Figure 58, shown in Figure 59, reveals the appearance of additional modes. These modes are spaced at twice the expected rate (0.248 nm) of the modes that appear with higher reverse voltages of -2 V, -2.5 V and -3 V.

The optical spectrum suffers a dramatic change when the reverse bias on the saturable absorber decreases below -2 volts, where the spectrum develops many stable modes in four different zones of the spectrum. The most remarkable point comes around 1580 nm (Figure 60), where the modes have a greater gain, and a zoomed graphic is presented in Figure 61. Three more gain areas appear around 1540, 1550 and 1570 nm, although they cannot be considered of any importance yet.

The previous spectrums share a common problem for the measurements in the laboratory. It seems that mode-locking can be present, but the power is not enough to make the measurements on an autocorrelator. Furthermore, the laboratory's amplifiers do not cover this emission band, so at this point it was impossible to progress.
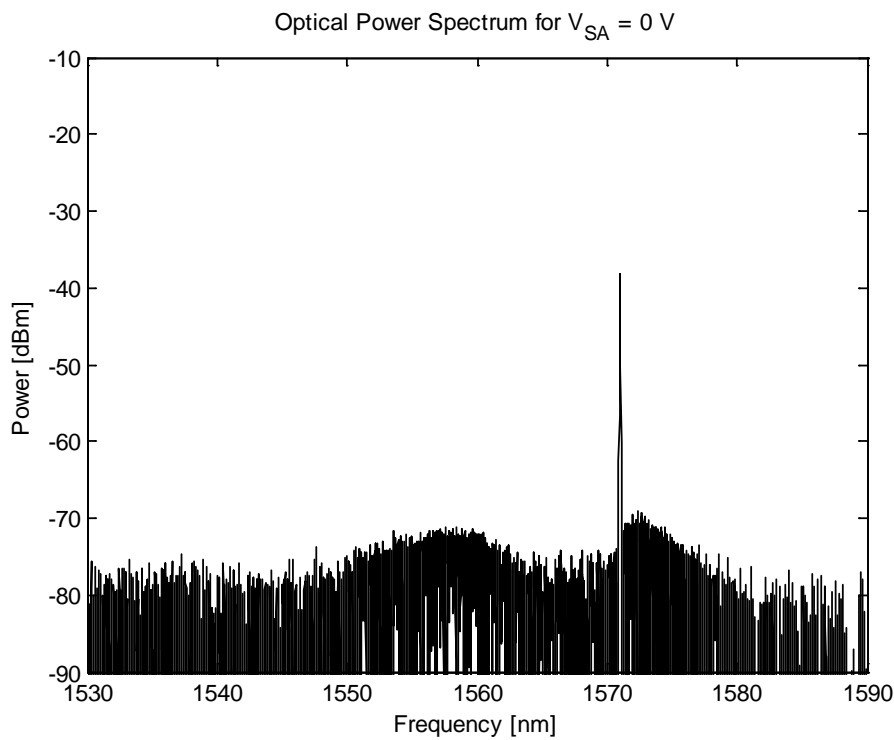
Figure 55. Optical spectrum for V_{SA} = 0 V

Optical Power Spectrum for V_{SA} = -0.5 V
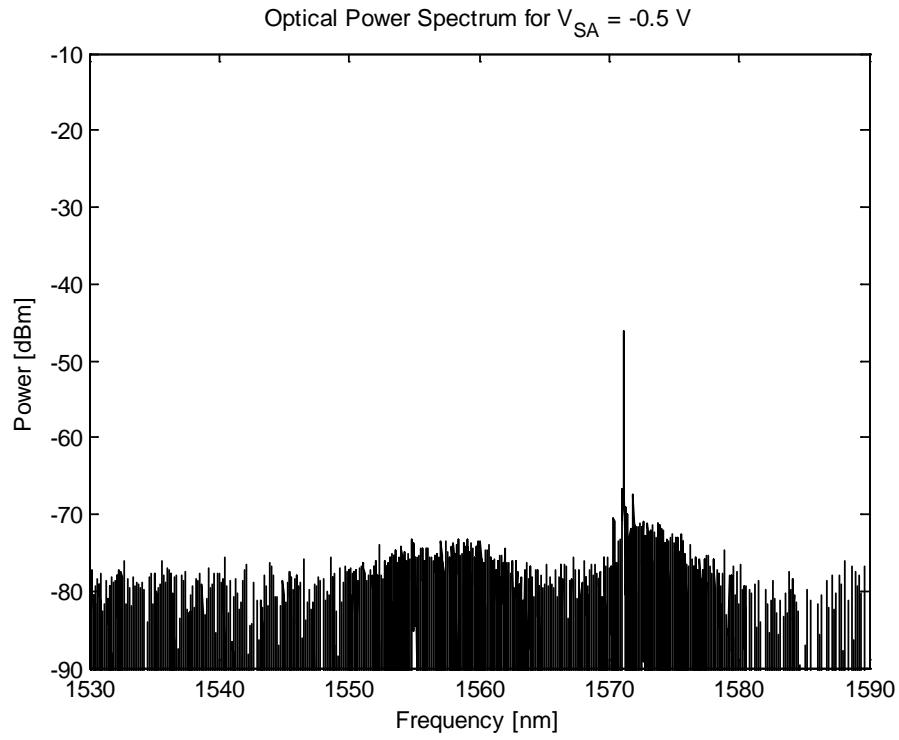
Figure 56. Optical spectrum for V_{SA} = -0.5 V

Optical Power Spectrum for V_{SA} = -1 V
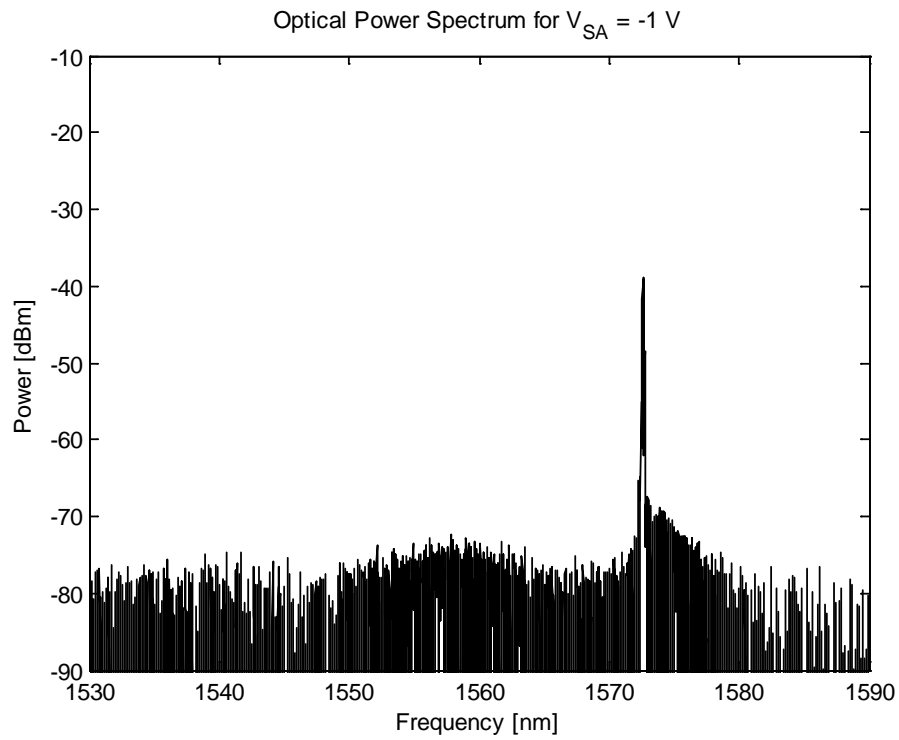
Figure 57. Optical spectrum for V_{SA} = -1 V

Optical Power Spectrum for V_{SA} = -1.5 V
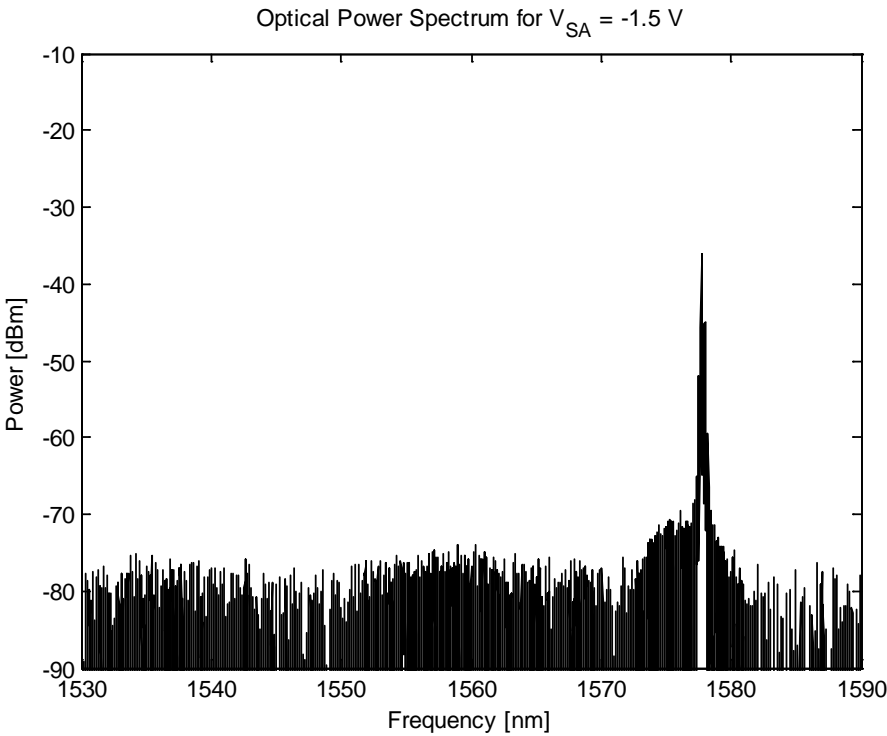
Figure 58. Optical spectrum for V_{SA} = -1.5 V

Zoom for Optical Power Spectrum for V_{SA} = -1.5 V
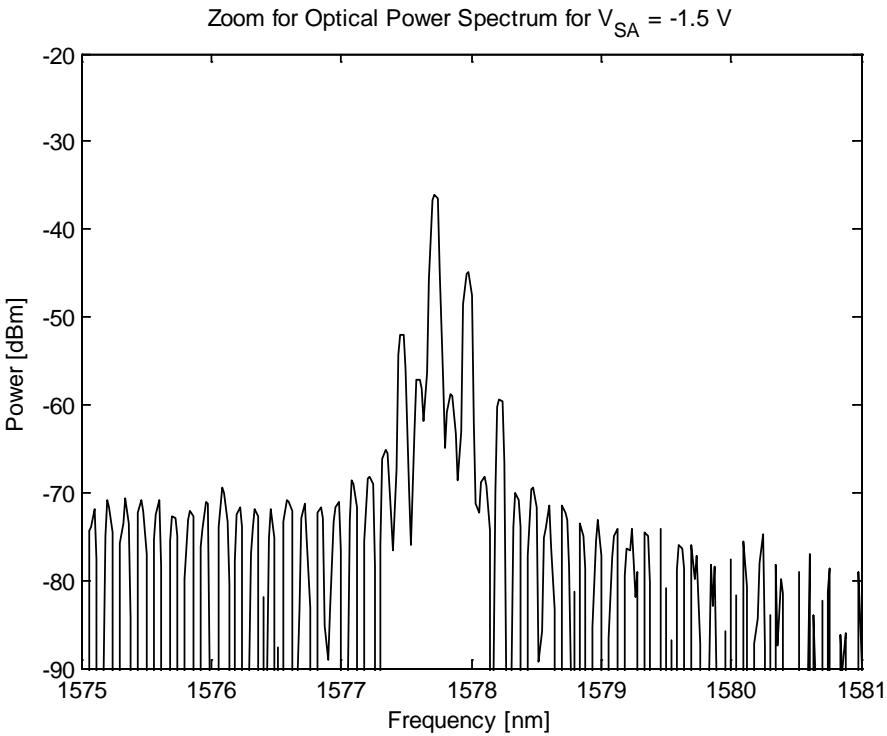
Figure 59. Zoom of the optical spectrum for V_{SA} = -1.5 V

Optical Power Spectrum for V_{SA} = -2 V
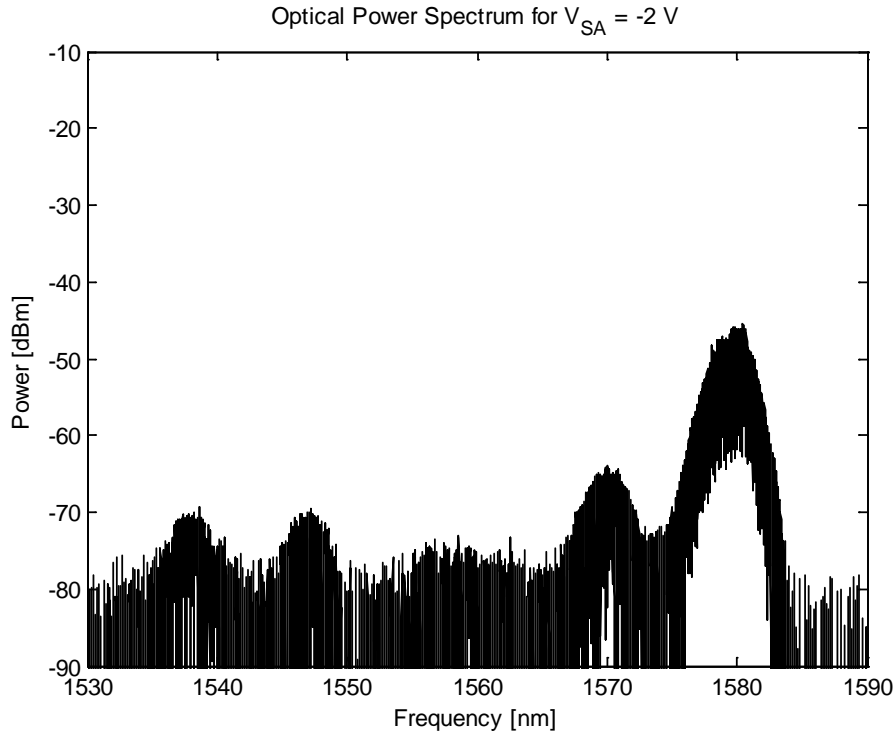
Figure 60. Optical spectrum for V_{SA} = -2 V

Zoom for Optical Power Spectrum for V_{SA} = -2 V
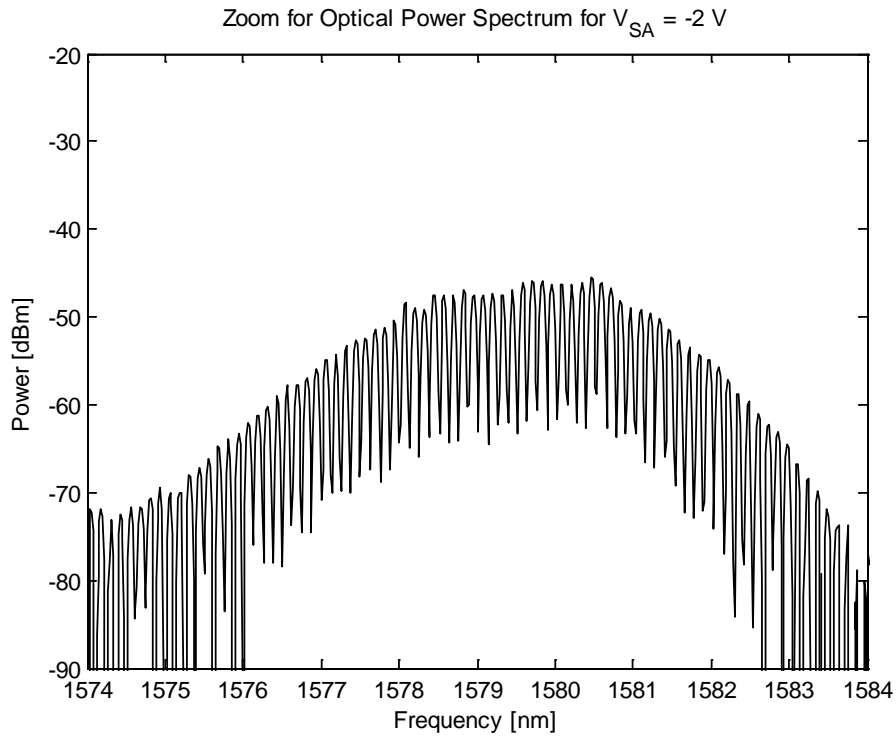
Figure 61. Zoom of the optical spectrum for V_{SA} = -2 V

Once the voltage was increased until -2.5 volts in the saturable absorber contact, the device switched its gain to a new area as it is observed in Figure 62. The 1570 and 1580 nm zones lose a great quantity of power, yielding it to the area between 1550 and 1560 nm. When the measurement image is enlarged at this point, several stable and equispaced modes appear

(Figure 63). The separation is of 0.124 nm between all of them, which can be converted to frequency terms giving a result of 14.87 GHz and corresponding to the expected repetition rate of the mode-locking ring laser.

It is well known that lasers do not present the same characteristics when sweeping the parameters in an increasing or decreasing way. For this reason, the measurements were repeated sweeping the saturable absorber's voltage downwards instead of doing it in an increasing way. It is noticeable that the behaviour of the laser was different at some of the measured points, specifically at the reverse voltage of -2 V. This time, the spectrum appeared to have a much wider gain bandwidth being very similar to the spectrum of Figure 62, although the voltage applied was of -2 V instead of -2.5 V. This means that there is hysteresis for the laser, as the spectrum was maintained the same at -2 V. Once this value was decreased to -1.9 V and lower values, the measures taken were similar to the ones obtained in the measurements where the reverse voltage was increased.
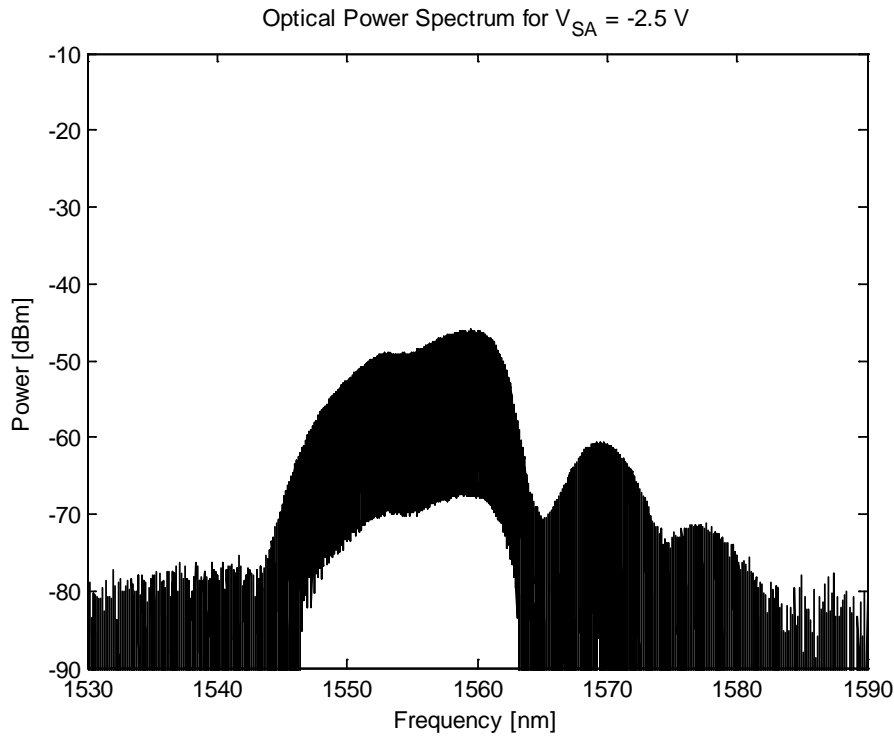
Figure 62. Optical spectrum for V_{SA} = -2.5 V

Zoom for Optical Power Spectrum for V_{SA} = -2.5 V
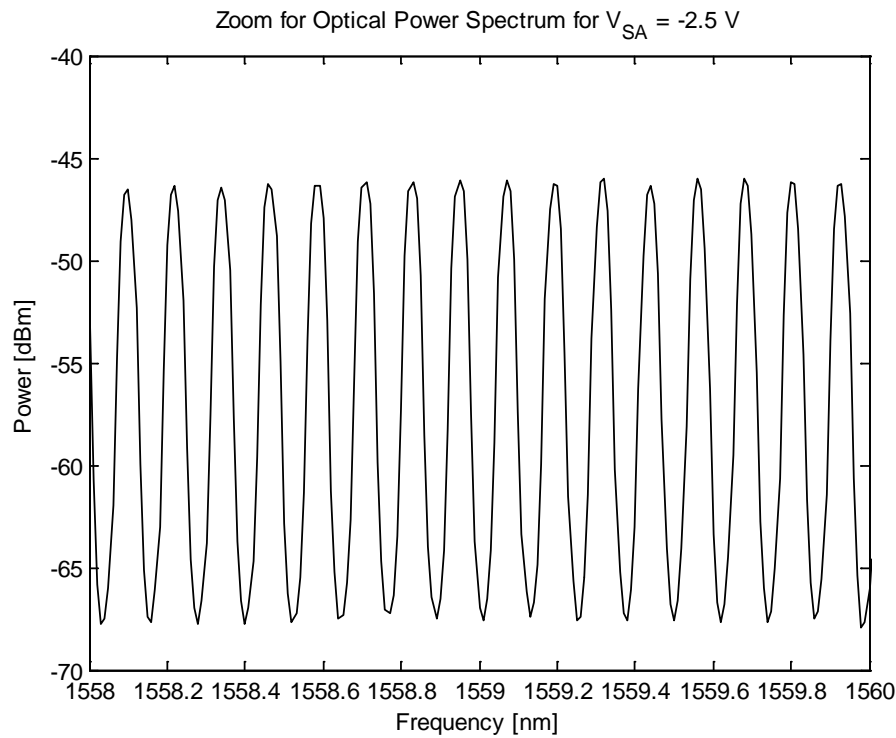
Figure 63. Zoom of the optical spectrum for V$_{SA}$ = -2.5 V

3.1.3. Radio Frequency Spectrum

As it was observed in the optical spectrum measurements, several equidistant modes were present at the laser optical output. Since these modes are phase locked, the optical output has a pulsed character. When the optical signal is taken to a high speed photodiode, we can observe on an RF spectrum analyser (RFSA) the spectrum of the electrical envelope.

3.1.3.1. Setup

The high speed photodiode has a maximum input power, that when surpassed, the device is destroyed. Since we need amplification of the laser output, we need to keep track of the power delivered to the photodiode at all times. Thus, a 90/10 coupler was inserted, directing 10% of the power towards the power meter and the resting 90% was amplified by the two EDFAs in series.

The amplified output, with a total power of 0 dBm, was introduced into a photodetector U2T XPDV2020R as the one seen in Figure 64 and later amplified by a CERNEX CBL02403050 RF Amplifier with a bandwidth of 40 GHz.
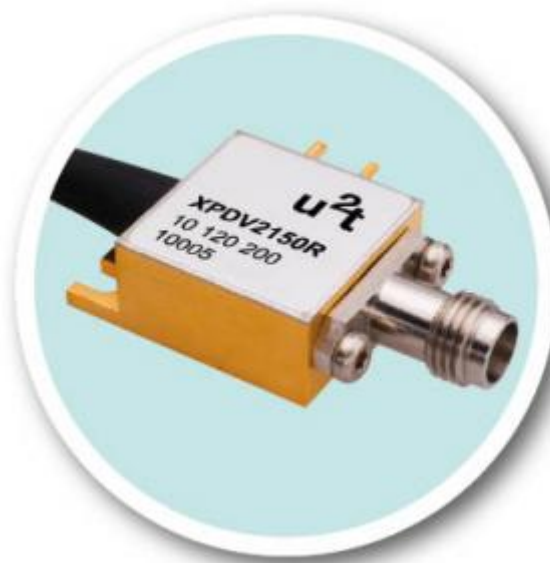
Figure 64. U2T Photodetector

3.1.3.2. Results

As it was expected, a radio frequency tone appeared near the frequency that had been previously determined with the optical spectrum analyser, exactly at 14.98 GHz. Two measurements of the spectral tone are showed in Figure 65 and Figure 66 with different SPAN values.
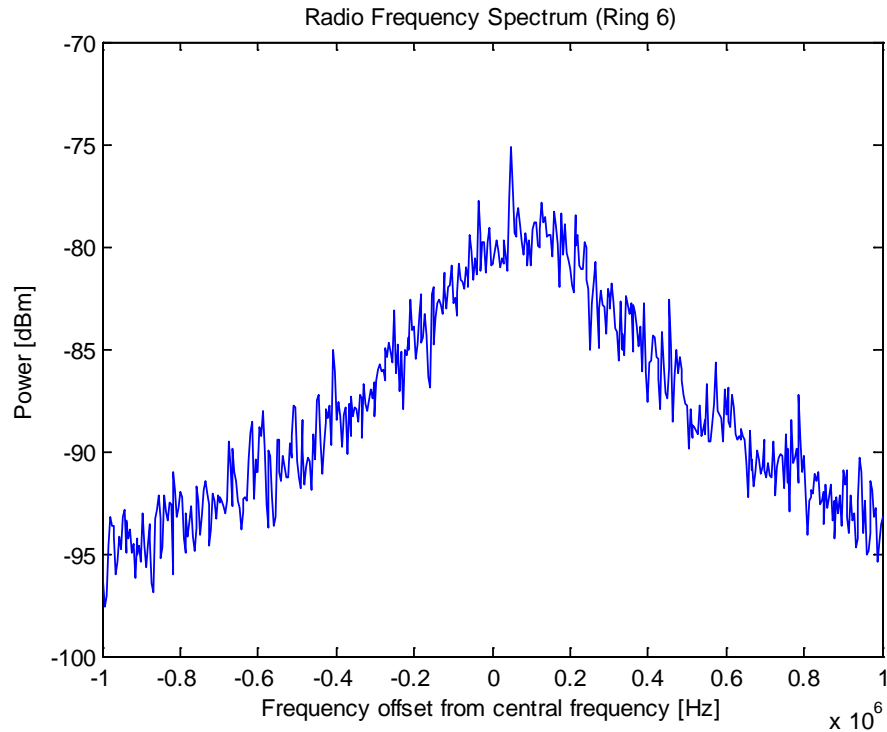
Figure 65. Radio Frequency Spectrum of Ring 6 with a SPAN of 2 MHz
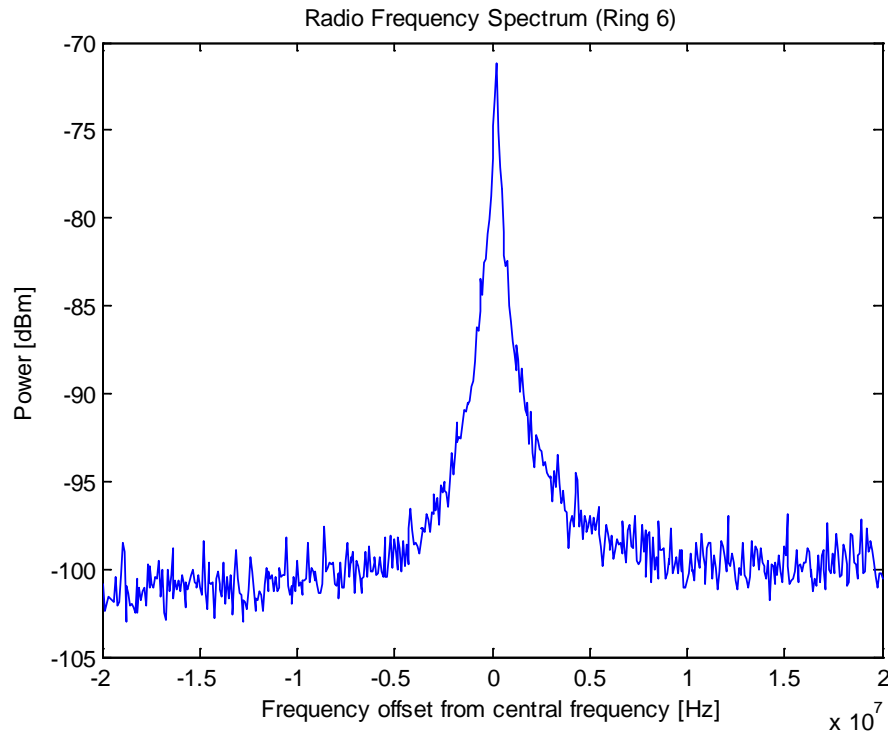
Figure 66. Radio Frequency Spectrum of Ring 6 with a SPAN of 40 MHz

Thanks to the Phase Noise Characterization interface, it has been possible to measure the phase noise of the ring laser under study. Three intervals were used in the configuration of the interface, written in Table 3.

Table 3. SPAN - RBW configuration for phase noise measurement

Measurement number	SPAN [MHz]	RBW [Hz]
1	2	1000
2	40	3000
3	400	10000

The signal received at the electrical spectrum analyser had a very low level, with a peak of -70 dBm. If we consult the datasheet of the measurement instrument [34], it is indicated that the noise floor is located at -105 dBm for a RBW of 1 KHz, or equivalently -135 dBm/Hz. Note that the values in Figure 67 decrease up to -65 dBm/Hz, which added to the peak power value of -70 dBm, gives the total value of the limiting noise floor of the spectrum analyser. In conclusion, this measurement did not result as expected due to the lack of power which limits the result.
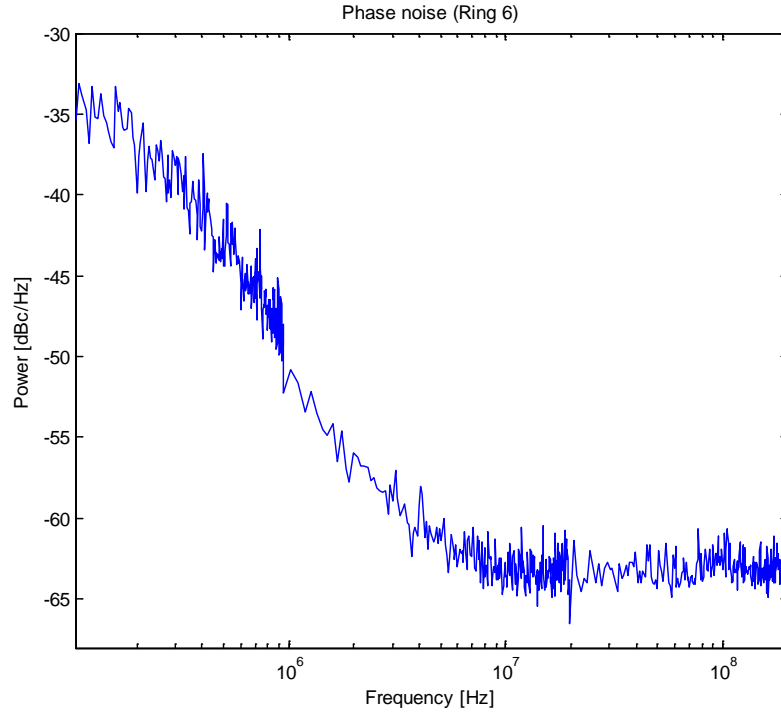
Figure 67. Phase Noise for Symmetric Ring Laser

3.1.4. Autocorrelation

There is only one measurement that proves that the device is in a mode locked regime. The autocorrelation measurement actually obtains an indirect measure of the pulse shape. By means of the autocorrelator of APE Photonics and the Pulse Autocorrelation interface, it was proved the existence of light pulses at the output of the laser and those pulses were studied.

3.1.4.1. Setup

The laser current conditions were varied around the optimal working point to investigate the changes over the emitted pulses. The applied currents on each probe are varied from 45 mA to 65 mA in steps of 5 mA, with the only condition that the total injected current is 110 mA, so that $I_{profile} + I_{ILX}$ = 110 mA. This allows us to unbalance the currents on the two gain sections, while we keep constant the total injected power. Moreover, the saturable absorber's voltage was also varied between -2.4 and -2.6 V for each combination.

To monitor the output power throughout the measurements, the laser's output was again split with the 10/90 coupler to visualize a small portion in the power meter while the rest was amplified with the two EDFAs and introduced into the autocorrelator. With the help of a polarizer, the light was correctly adapted to maximize the signal in the interferometer.

3.1.4.2. Pulsewidth evolution

Once it was checked the existence of light pulses at the CCW output of the laser, it was considered important to observe how the pulse profile and temporal width developed for a series of varying parameters. In order to illustrate this study, the measurements are presented for an increasing voltage parameter for the saturable absorber probe going from -2.4 to -2.6 V.

For each case, different currents are shown for each probe, the pulses' profile and their evolution.

A span of 50 ps has been employed to capture the whole pulse autocorrelation trace, as the next option was to use a 15 ps one which was too small. Three measurements are made for each working point to ensure the measured values.

3.1.4.2.1. VSA = -2.4 V

The first autocorrelation measurement of the laser's pulses has the following conditions of current in its probes:

$$I_{profile} = 45 \; mA$$

$$I_{ILX} = 65 \; mA$$

The measured autocorrelation trace was obtained through the designed interface. From the autocorrelation shape, a further processing step is necessary to fit the best lineshape for the pulse and obtain the pulse width. Figure 68 shows the first measurement of the autocorrelation trace with the three fitting models represented graphically.
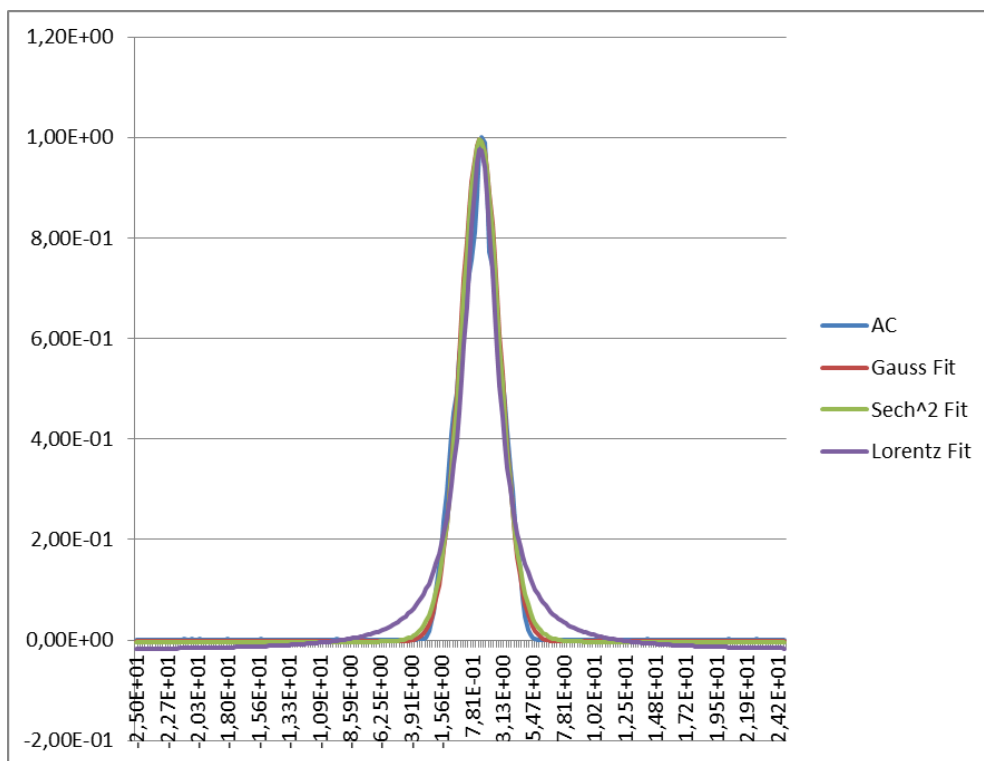
Figure 68. Data fitting for the autocorrelation trace

Taking a look back at Table 2, it can be remembered that the three most important pulse shapes where the ones present in Table 4, which shows a table with the models' parameters which fit best the measured autocorrelation trace. The objective of fitting these models to the autocorrelation trace is to determine the temporal width of the light pulse emitted by the ring laser. The last row of Table 4 determines the hypothetical pulsewidth depending on the fitting model. The model that best fits the pulse is selected by the resulting quadratic error, being in this case the Sech^2 fit.

Table 4. Fit parameters for autocorrelation trace

Gaussian Fit		Sech^2 Fit		Lorentzian Fit	
time offset	1,420739	time offset	1,425634	time offset	1,448071
pulse width	1,51858	pulse width	1,277959	pulse width	0,7804454
Y offset	-0,00306	Y offset	-0,003604	Y offset	-0,021092
Error	0,154339	Error	0,14013	Error	0,3347934

Tpw [ps]	2,528602	Tpw [ps]	2,252658	Tpw [ps]	1,5608908

To avoid repeating all of the parameters, only the selected fit's parameters will be shown in Table 5. Three measurements were made for each working point to ensure the obtained values. In summary, a graphic (Figure 69) is plotted to show the most important parameters obtained. The temporal pulse width changes considerably with current injection, as well as the pulses' shape.

If the mean temporal width of each three measurements is taken, it is clear which points are the ones with the lower pulse width as it is seen in Figure 70.

Table 5. Autocorrelation measurements for V_{SA} = -2.4 V

V_{SA} [V]	I_{ILX}	$I_{profile}$	t_{offset} [ps]	AC width [ps]	Error	Fit model	TPW [ps]
-2.4	45	65	1.43	1.28	0.140130	Sech^2	2.2527
-2.4	45	65	1.41	1.30	0.137791	Sech^2	2.2841
-2.4	45	65	1.43	1.29	0.131840	Sech^2	2.2706
-2.4	50	60	1.38	1.40	0.281847	Sech^2	2.4621
-2.4	50	60	1.37	1.42	0.265077	Sech^2	2.5014
-2.4	50	60	1.37	1.44	0.216212	Sech^2	2.5456
-2.4	55	55	0.56	0.61	0.326759	Lorentzian	1.2220
-2.4	55	55	0.58	0.60	0.300158	Lorentzian	1.2048
-2.4	55	55	0.52	0.64	0.300069	Lorentzian	1.2792
-2.4	60	50	0.54	0.62	0.338027	Lorentzian	1.2450
-2.4	60	50	0.56	0.51	0.278424	Lorentzian	1.0163
-2.4	60	50	0.57	0.55	0.332432	Lorentzian	1.0907
-2.4	65	45	1.44	1.13	0.281795	Sech^2	1.9980
-2.4	65	45	1.43	1.17	0.246258	Sech^2	2.0638
-2.4	65	45	1.43	1.18	0.237198	Sech^2	2.0728
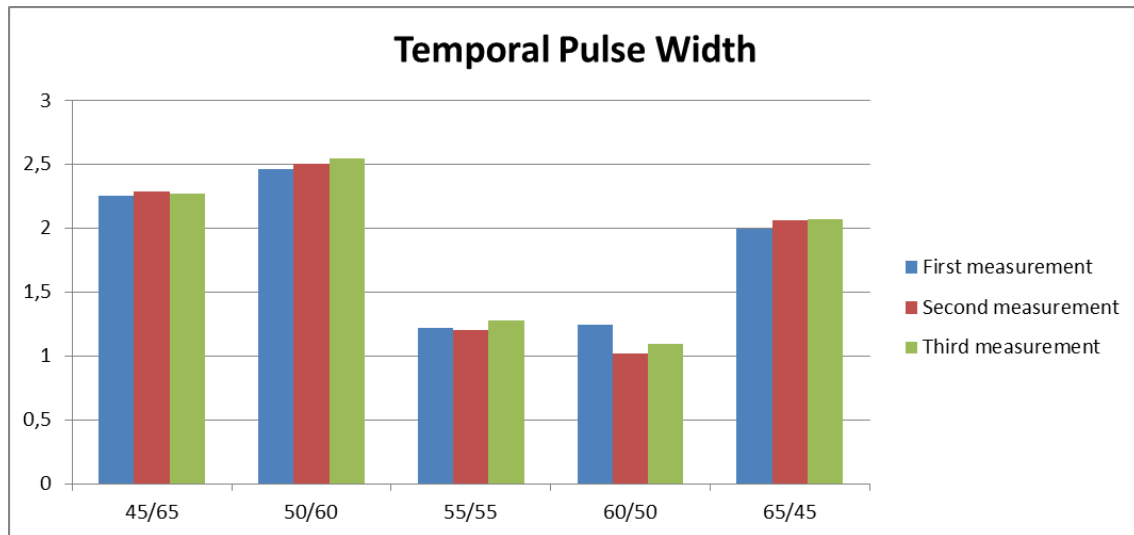
Figure 69. Temporal width of the measured pulses for V_{SA} = -2.4 V
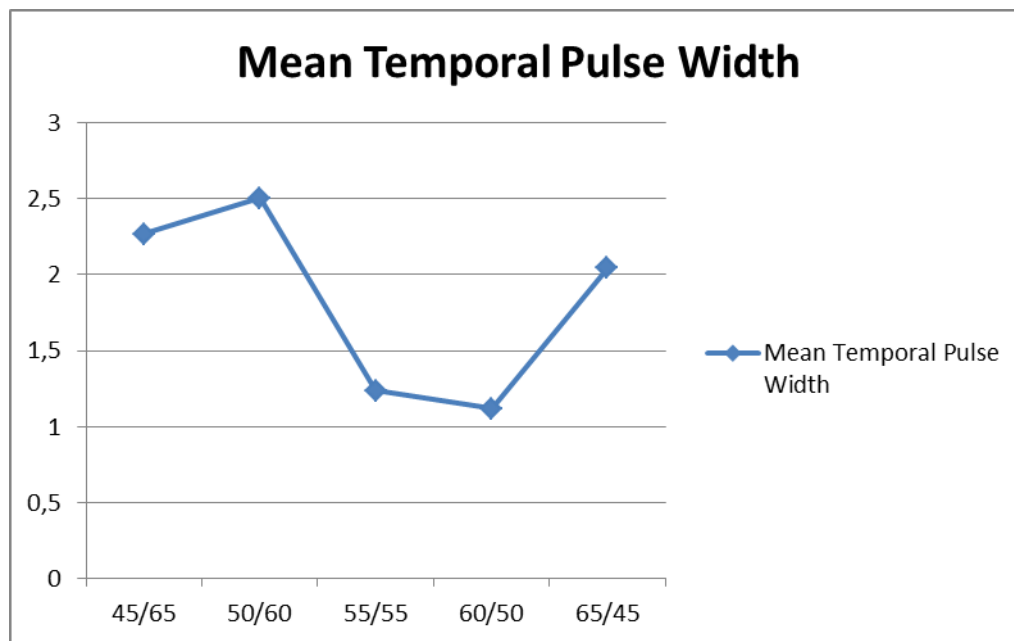
Figure 70. Mean temporal width evolution for V_{SA} = -2.4 V

3.1.4.2.2. V_{SA} = -2.5 V

As it has been done for the previous voltage, the same analysis is now presented for V_{SA}=-2.5 V. The corresponding results are noted in Table 6.

Similarly to what was observed before, the pulses fit to different models depending on the current injection on every voltage step. Results are shown graphically in Figure 71 and Figure 72, including a new point where pulses fit a Lorentzian trace. From this fact, it can be extracted that voltage also influences in the laser emitted pulses.

Table 6. Autocorrelation measurements for V_{SA} = -2.5 V

V_{SA} [V]	I_{ILX}	$I_{profile}$	t_{offset} [ps]	AC width [ps]	Error	Fit model	TPW [ps]
-2.5	45	65	1.45	0.63	0.285241	Lorentzian	1.2671
-2.5	45	65	1.47	0.63	0.299072	Lorentzian	1.2505
-2.5	45	65	1.47	0.61	0.280069	Lorentzian	1.2174
-2.5	50	60	1.39	1.42	0.268581	Sech^2	2.5027
-2.5	50	60	1.38	1.46	0.252983	Sech^2	2.5780
-2.5	50	60	1.38	1.43	0.262994	Sech^2	2.5287
-2.5	55	55	0.56	0.61	0.310029	Lorentzian	1.2248
-2.5	55	55	0.56	0.53	0.309437	Lorentzian	1.0637
-2.5	55	55	0.57	0.50	0.343248	Lorentzian	0.9934
-2.5	60	50	0.52	0.64	0.372912	Lorentzian	1.2879
-2.5	60	50	0.56	0.68	0.372877	Lorentzian	1.3589
-2.5	60	50	0.58	0.61	0.347494	Lorentzian	1.2278
-2.5	65	45	1.42	1.28	0.176528	Sech^2	2.2552
-2.5	65	45	1.42	1.25	0.207087	Sech^2	2.1977
-2.5	65	45	1.41	1.28	0.181477	Sech^2	2.2586

Figure 71. Temporal width of the measured pulses for V_{SA} = -2.5 V

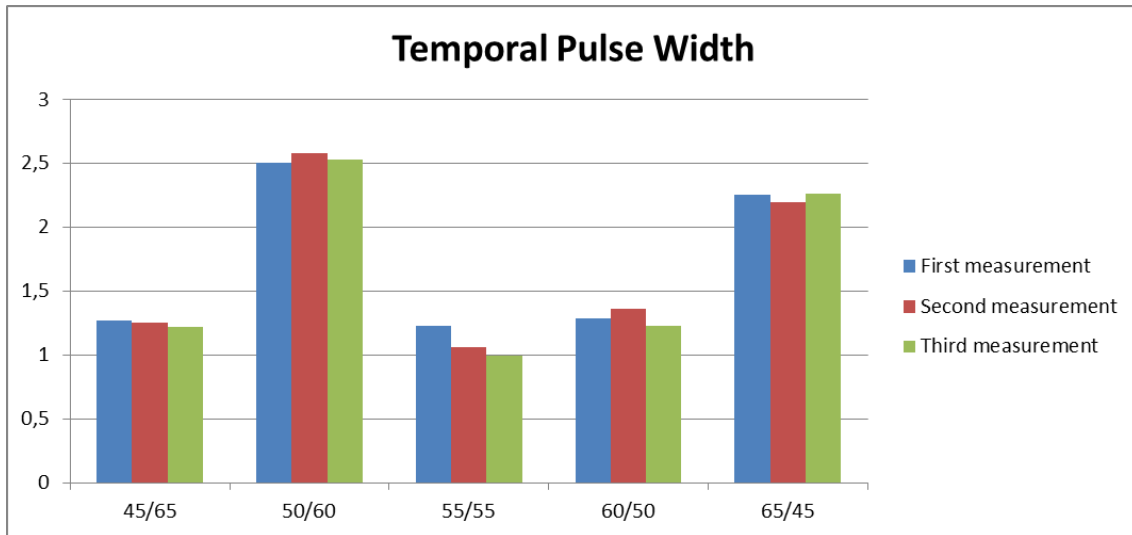**Figure 72. Mean temporal width evolution for V$_{SA}$ = -2.5 V**
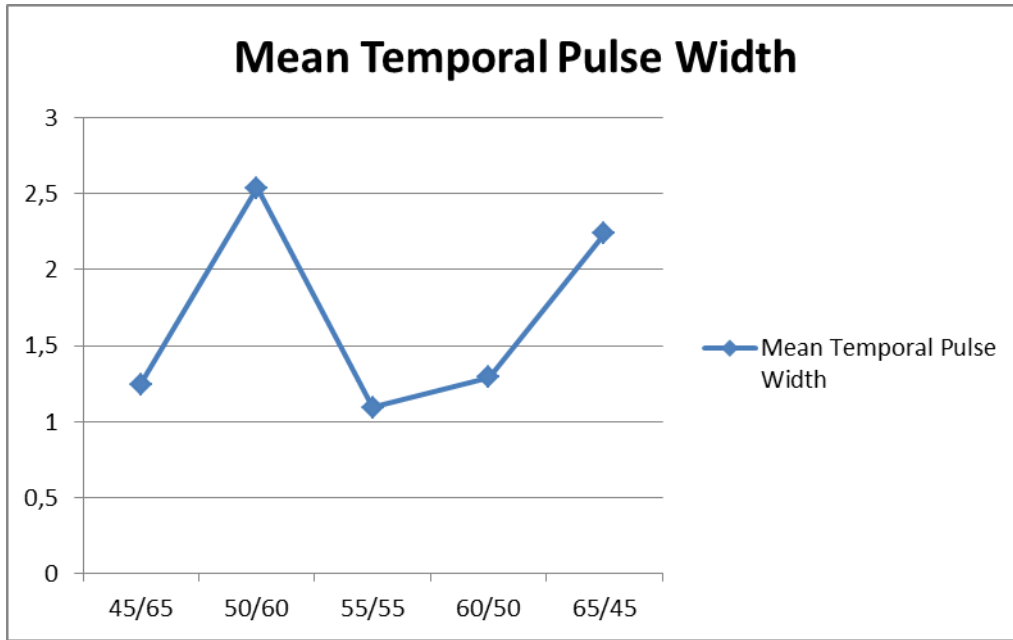
3.1.4.2.3.   V$_{SA}$ = -2.6 V

Again, the results of measuring the pulses under a voltage of -2.6 V are captured in Table 7.

These last measurements corroborate the results seen throughout the autocorrelation study. Through the saturable absorber's inverse voltage and the individual current probes, the shape of the pulse can be controlled.

A clear tendency must be remarked in Figure 73 and Figure 74. As the injected current is increased in the I$_{profile}$ probe and reduced in the I$_{ILX}$ one, light pulses get narrower. This is a very interesting result, as it proves that the shape and width of the pulses can be controlled through an asymmetric bias.

Table 7. Autocorrelation measurements for V$_{SA}$ = -2.6 V

V$_{SA}$ [V]	I$_{ILX}$	I$_{profile}$	t$_{offset}$ [ps]	AC width [ps]	Error	Fit model	TPW [ps]
-2.6	45	65	1.43	0.66	0.284312	Lorentzian	1.3245
-2.6	45	65	1.40	1.15	0.265313	Sech^2	2.0219
-2.6	45	65	1.46	0.66	0.272357	Lorentzian	1.3279
-2.6	50	60	1.38	1.48	0.221836	Sech^2	2.6013
-2.6	50	60	1.39	1.41	0.261360	Sech^2	2.4837
-2.6	50	60	1.37	1.45	0.235915	Sech^2	2.5534
-2.6	55	55	0.52	0.60	0.446933	Lorentzian	1.1988
-2.6	55	55	0.55	0.62	0.455585	Lorentzian	1.2345
-2.6	55	55	0.57	0.74	0.426967	Lorentzian	1.4749

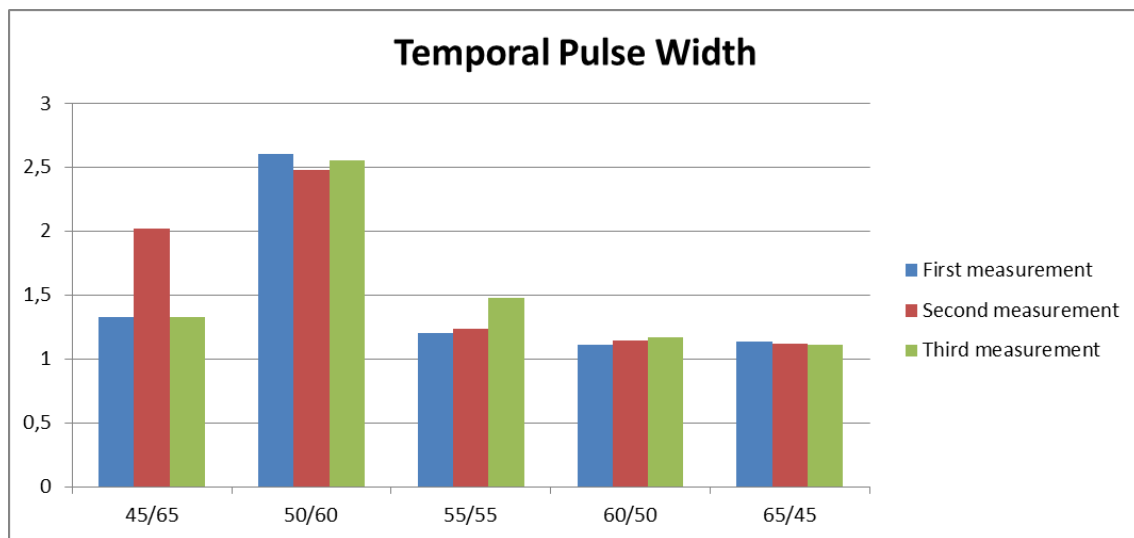| -2.6 | 60 | 50 | 0.60 | 0.56 | 0.369151 | Lorentzian | 1.1128 |
-2.6	60	50	0.60	0.57	0.386060	Lorentzian	1.1453
-2.6	60	50	0.60	0.58	0.357512	Lorentzian	1.1649
-2.6	65	45	1.50	0.57	0.314332	Lorentzian	1.1383
-2.6	65	45	1.51	0.56	0.317175	Lorentzian	1.1198
-2.6	65	45	1.50	0.55	0.323781	Lorentzian	1.1088

Figure 73. Temporal width of the measured pulses for V_{SA} = -2.6 V
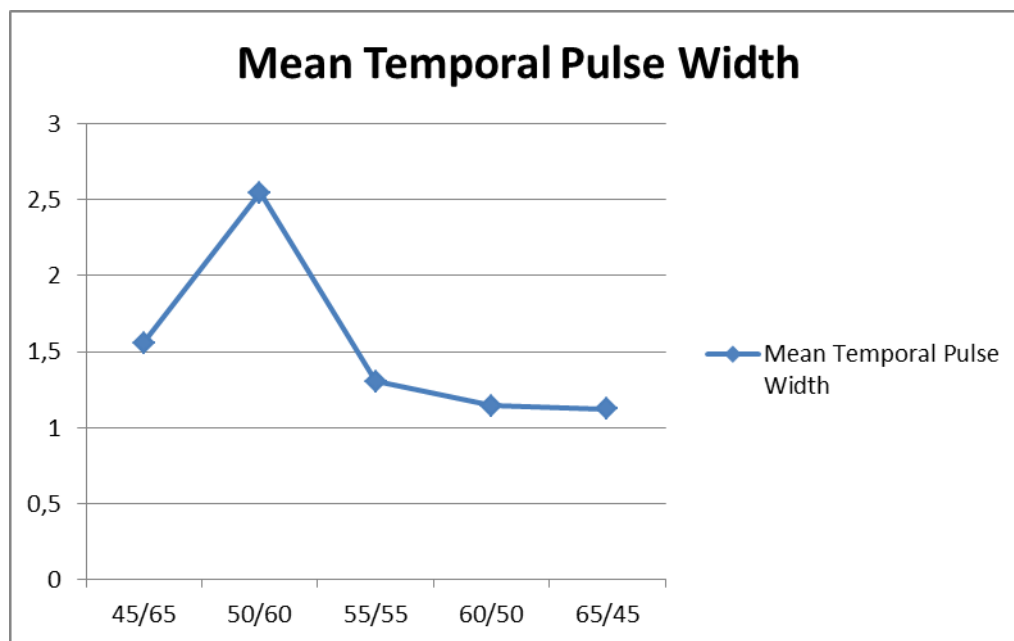

Figure 74. Mean temporal width evolution for V_{SA} = -2.6 V

Chapter 4

Conclusions and future lines

The present project has analysed photonic integrated mode locked sources, designed at the Universidad Carlos III de Madrid and fabricated within the European InP JePPIX platform. The interest of these devices lies in their potential to be integrated with other optical components into a Photonic Integrated Circuit, as the ring laser structure is not restricted by the need to have cleaved facets to create the laser resonator; therefore the light is coupled to waveguides within the chip. Mode locked lasers produce short pulses of light periodically, which can be used within applications that need a precise clock, such as all optical clock extraction in optical time division multiplexing (OTDM).

This project has developed three different interfaces to interact with the laboratory instruments over two different platforms. Two interfaces were developed within LabView, and another on Matlab. With the help of these tools, several ring lasers were measured, taking the most adequate results to the third chapter of this document.

The first interface that we present in this project takes the light versus current characteristics (PI curves). Measurements on one of the ring configurations are presented, which is a symmetric ring laser with two sections of gain and a saturable absorber. The dependence of this characteristic traces were measured with increasing voltages of the saturable absorber, with particular attention to the interaction among the two different counter-propagating directions of the ring. For voltages of the saturable absorber above -1.5 V, the laser presents the typical bistability between its CW and CCW modes. When this parameter goes below -2 V, the behaviour of the laser changes, showing the PI curves a dominance of the CCW. From this point, it is clear that the voltage applied to a symmetric saturable absorber in a symmetric structured device can control its behaviour and induce a new working regime. Moreover, the best working points were extracted from these results to continue with the next steps in the study.

We have analysed as well the optical spectrum for selected bias conditions identified on the PI traces, observed on an Optical Spectrum Analyser. We identified that at lower voltages, only one mode is present. At -1.5 V, the spectrum shows a total of 4 modes in a very narrow bandwidth, although they are not stable and so mode-locking cannot appear. A great change is identified at the reverse bias voltage of -2 V. Several modes appear over a broad gain bandwidth, although this band is located around 1580 nm. When the value of -2.5 V is reached, the gain switches its area to a wider bandwidth which is located between 1545 and 1565 nm. Well-defined and equispaced modes can be observed in the spectrum analyser, so the hypothesis of being in a mode-locking regime is presented. The same situation is given for the final value of -3 V in the saturable absorber.

When the device operates on a mode-locked regime, its modes beat among themselves generating a RF signal at a frequency determined by their mode spacing when the optical output is shined on a high speed photodiode. The second interface that we have developed in this study analyses the characteristics of this generated electrical signal on a Radio Frequency Spectrum Analyser (RFSA) scope. Once the best working point is selected thanks to the measurements made up to here, the laser output was connected to a photodetector which captured the signal to be analysed. A tone was found at a frequency very close to the one expected from the theoretical design, 14.98 GHz. Although the results were not as good as expected due to the lack of power received at the analyser, the phase noise of the signal could be measured.

Having observed this signal, it was clearer that the laser's output was pulsed. However, a last characterization of the emitted pulses could be made with the autocorrelation measurement tools as it was justified in the first chapter. These results are the most important ones, as they are the first measured pulses from this chip of ring lasers.

At first glance, it must be remarked that the emitted pulses are of a very short duration, which is a promising result. Most of the measured pulses had a temporal estimated width between 1 and 2 picoseconds, adjusting them to three different pulse shapes: Gaussian, Lorentzian and Sech2. The number of positive matches was distributed between the Lorentzian and Sech2 models, not having measured any with Gaussian shape. In this case, the Lorentzian profile was preferred, as it offered narrower pulses for the same autocorrelation trace.

This same year in Eindhoven, it was demonstrated experimentally for the first time to our knowledge that the relative positioning of the amplifier and absorber in a monolithically integrated ring laser can be used to control the balance of power between counter-propagating fields in the mode-locked state. This work was carried out on an asymmetric ring cavity with a single SOA section and an asymmetric saturable absorber. For this project, a symmetric structure with two SOA sections and a single and centred saturable absorber was employed. It has been demonstrated, also for the first time to our knowledge, that the shape of the emitted pulses in the mode-locked state can be controlled through an asymmetric bias.

The future lines of this project are centred in a more detailed study of the mode-locked regime. The measurements of the optical and radio frequency spectrums can be automated to create maps, in which the evolution of the spectrums can be represented easily.

Budget

The project has been developed in three main stages. The first one has consisted in the study and simulation of different laser structures. The development of the interfaces of PI characterization and Phase noise measurement was the next step before making the study of the provided ring lasers. As a last stage, the autocorrelation study of the laser emitted pulses was made.

All these stages are shown in the temporal line of the Gantt diagram of Figure 75.

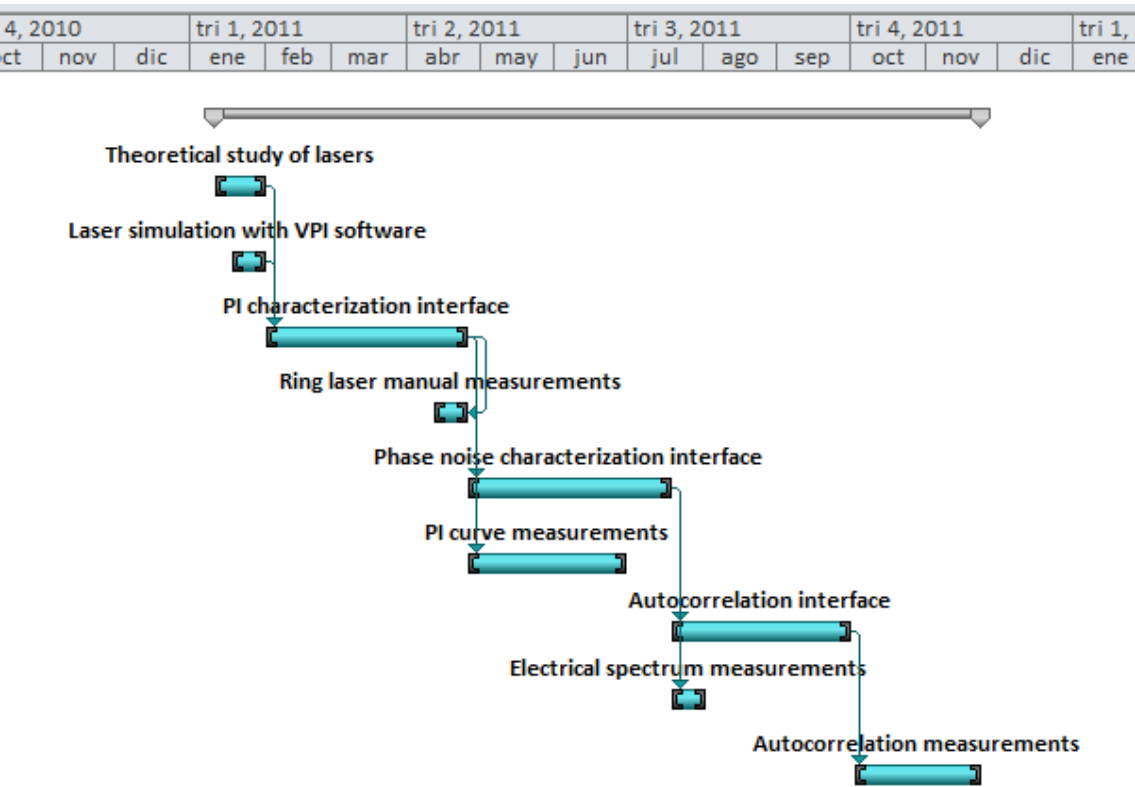Figure 75. Project's Gantt diagram

The project costs are detailed in the budget sheet of <u>page 71</u>, concluding that the total cost of the present project is of 39,011.20 €.

Leganés, 9 December 2011

The project engineer

Álvaro Jimenez Galindo

UNIVERSIDAD CARLOS III DE MADRID
Escuela Politécnica Superior

PRESUPUESTO DE PROYECTO

1.- Autor:
Álvaro Jiménez Galindo

2.- Departamento:
Tecnología Electrónica

3.- Descripción del Proyecto:
- Titulo: Caracterización de fuentes fotónicas de pulsos de luz integrables mediante diodos láser en anillo enganchados e
- Duración (meses): **11**
- Tasa de costes Indirectos: **20%**

4.- Presupuesto total del Proyecto (valores en Euros):
39.011,20 Euros

5.- Desglose presupuestario (costes directos)

PERSONAL

Apellidos y nombre	N.I.F. (no rellenar - solo a titulo informativo)	Categoría	Dedicación (hombres mes) a)	Coste hombre mes	Coste (Euro)	Firma de conformidad
					0,00	
Carpintero del Barrio, Guillermo		Ingeniero Senior	0,69	4.289,54	2.959,78	
Jiménez Galindo, Álvaro		Ingeniero	5,19	2.694,39	13.983,88	
					0,00	
					0,00	
		Hombres mes 5,88		**Total**	16.943,67	

a) 1 Hombre mes = 131,25 horas. Máximo anual de dedicación de 12 hombres mes (1575 horas)
   Máximo anual para PDI de la Universidad Carlos III de Madrid de 8,8 hombres mes (1.155 horas)

EQUIPOS

Descripción	Coste (Euro)	% Uso dedicado proyecto	Dedicación (meses)	Periodo de depreciación	Coste imputable d)
ILX Lightwave Diode Controller	4.000,00	100	11	60	733,33
Profile Current source	6.000,00	100	11	60	1.100,00
HP Voltage source	3.000,00	100	11	60	550,00
Radio Frequency Spectrum Analy	86.000,00	100	4	60	5.733,33
Optical Spectrum Analyser	24.000,00	100	8	60	3.200,00
Photodetector u2t	3.000,00	100	4	60	200,00
APE Autocorrelator	12.000,00	100	4	60	800,00
				Total	12.316,67

d) Fórmula de cálculo de la Amortización:

$$\frac{A}{B} x C x D$$

A = nº de meses desde la fecha de facturación en que el equipo es utilizado
B = periodo de depreciación (60 meses)
C = coste del equipo (sin IVA)
D = % del uso que se dedica al proyecto (habitualmente 100%)

SUBCONTRATACIÓN DE TAREAS

Descripción	Empresa	Coste imputable
	Total	0,00

OTROS COSTES DIRECTOS DEL PROYECTO e)

Descripción	Empresa	Costes imputable
Matlab license		500,00
LabView license		2.749,00
	Total	3.249,00

e) Este capítulo de gastos incluye todos los gastos no contemplados en los conceptos anteriores, por ejemplo: fungible, viajes y dietas,

6.- Resumen de costes

Presupuesto Costes Totales	Presupuesto Costes Totales
Personal	16.944
Amortización	12.317
Subcontratación de tareas	0
Costes de funcionamiento	3.249
Costes Indirectos	6.502
Total	39.011

Glossary

AWG	Arrayed Waveguide Grating
CCW	Counter-clockwise
CPM	Colliding Pulse Mode
CPML	Colliding Pulse Mode-Locking
CW	Continuous Wave / Clockwise
EDFA	Erbium Doped Fibre Amplifier
FWHM	Full Width at Half Maximum
GPIB	General-Purpose Instrumentation Bus
GUI	Graphic User Interface
HML	Hybrid Mode-Locking
IF	Intermediate Frequency
InP JePPIX	Joint European Platform for Indium Phosphide based Photonic Integrated Components and Circuits
MMI	Multi Mode Interference
OE	Optical-Electrical
OS	Operating System
OSA	Optical Spectrum Analyser
OTDM	Optic Time Division Multiplexing
PCF	Peak Centre Frequency
PIC	Photonic Integrated Circuit
PML	Passive Mode-Locking
PMT	Photomultiplier
PRL	Peak Reference Level

RBW	Resolution Bandwidth
RF	Radio-Frequency
RFSA	Radio-Frequency Spectrum Analyser
RIN	Relative Intensity Noise
RS232	Recommended Standard 232
RTD	Resistance Temperature Detector
SA	Saturable Absorber
SHG	Second Harmonic Generation
SOA	Semiconductor Optical Amplifier
SSB	Single Side Band
TDM	Time Division Multiplexing
USB	Universal Serial Bus
UV	Ultraviolet
VISA	Virtual Instrument Software Architecture
WDM	Wavelength Division Multiplexing

Bibliography

T. Krauss, P. Laybourn and J. Roberts, "CW operation of semiconductor ring lasers," *Electronics Letters,* vol. 26, no. 25, pp. 2095-2097, 1990.

1]

J. P. Hohimer, D. C. Craft, G. R. Hadley, G. A. Vawter and M. E. Warren, "Single-frequency continuous-wave operation of ring resonator diode laser," *Applied Physics Letters,* vol. 59, pp. 3360-3362, 1991.

2]

P. B. Hansen, G. Raybon, M. D. Chien, U. Koren, B. I. Miller, M. G. Young, J. M. Verdiell and C. A. Burrus, "A 1.54-µm monolithic semiconductor ring laser: CW and mode-locked operation," *IEEE Photon Technology Letters,* vol. 4, pp. 411-413, 1992.

3]

J. P. Hohimer and G. A. Vawter, "Passive mode locking of monolithic semiconductor ring lasers at 86 GHz," *Applied Physics Letters,* vol. 63, no. 12, pp. 1598-1600, 1993.

4]

M. Smit, S. Oei, F. Karouta, R. Nötzel, J. Wolter, E. Bente, X. Leijtens, J. van der Tol, M. Hill, H. Dorren, D. Khoe and D. Binsma, "Photonic integrated circuits: where are the limits?," in *Integrated Photonics Research and Applications*, 2005.

5]

J. Carroll, J. Whiteaway and D. Plumb, Distributed feedback semiconductor lasers, SPIE Press, 1998.

6]

B. E. A. Saleh and M. C. Teich, Fundamentals of Photonics, John Wiley & Sons, 2007.

7]

C. de Dios, *Generación de Pulsos Cortos mediante Diodos Láser Gain Switching. Estudio de Técnicas de Compresión Experimental basadas en Lazos Ópticos no Lineales NOLM,* Madrid, 2010.

8]

G. P. Agrawal and N. K. Dutta, Semiconductor Lasers, New York: Van Nostrand Reinhold, 1986.

9]

M. Sorel, G. Giuliani, A. Scire, R. Miglierina, S. Donati and P. Laybourn, "Operating regimes of GaAs-AlGaAs semiconductor ring lasers: experiment and model," *IEEE Journal of Quantum Electronics,* vol. 39, no. 10, pp. 1187-1195, October 2003.

10]

R. Burton, T. Schlesinger and M. Munowitz, "An investigation of the modal coupling of simple branching semiconductor ring lasers," *Journal of Lightwave Technology,* vol. 12, no. 5, pp. 754-759, May 1994.

11]

T. F. Krauss, R. De La Rue and P. J. R. Laybourn, "Impact of output coupler configuration on operating characteristics of semiconductor ring lasers," *Journal of*

12]

Lightwave Technology, vol. 13, no. 7, pp. 1500-1507, July 1995.

13]
R. v. Roijen, E. C. M. Pennings, M. J. N. van Stalen, T. van Dongen, B. H. Verbeek and J. M. M. van der Heijden, "Compact InP-based ring lasers employing multimode interference couplers and combiners," *Applied Physics Letters,* vol. 64, no. 14, pp. 1753-1755, 1994.

14]
T. Krauss, R. M. De La Rue, I. Gontijo, P. J. R. Laybourn and J. S. Roberts, "Strip-loaded semiconductor ring lasers employing multimode interference output couplers," *Applied Physics Letters,* vol. 64, no. 21, pp. 2788-2790, 1994.

15]
E. Pennings, R. van Roijen, M. van Stralen, P. de Waard, R. Koumans and B. Verbeck, "Reflection properties of multimode interference devices," *IEEE Photonics Technology Letters,* vol. 6, no. 6, pp. 715-718, 1994.

16]
H. Shams, A. Kaszubowska-Anandarajah, P. Perry and L. Barry, "Demonstration and optimization of an optical impulse radio ultrawideband distribution system using a gain-switched laser transmitter," *Journal of Optical Networking,* vol. 8, no. 2, pp. 179-187, 2009.

17]
K. Yvind, D. Larsson, L. Christiansen, J. Mork, J. Hvam and J. Hanberg, "High-performance 10 GHz all-active monolithic modelocked semiconductor lasers," *Electronics Letters,* vol. 40, no. 12, pp. 735-737, 2004.

18]
E. Avrutin, J. Marsh and E. Portnoi, "Monolithic and multi-gigahertz mode-locked semiconductor lasers: constructions, experiments, models and applications," *IEEE Proceedings - Optoelectronics,* vol. 147, no. 4, pp. 251-278, 2000.

19]
T. Shimizu, I. Ogura and H. Yokoyama, "860 GHz rate asymmetric colliding pulse modelocked diode lasers," *Electronics Letters,* vol. 33, no. 22, pp. 1868-1869, 1997.

20]
R. Kaiser and B. Huttl, "Monolithic 40-GHz Mode-Locked MQW DBR Lasers for High-Speed Optical Communication Systems," *IEEE Journal of Selected Topics in Quantum Electronics,* vol. 13, no. 1, pp. 125-135, 2007.

21]
M. Kroh, "Semiconductor mode-locked laser for high-speed OTDM Transmission," Berlin, 2006.

22]
Y. Barbarin, *1.55 μm Integrated Modelocked Semiconductor Lasers,* Eindhoven: TU Eindhoven, 2007.

23]
P. Vasilev, Ultrafast diode lasers: fundamentals and applications, Artech House, 1995.

24]
E. Bente, *Unravelling high-speed optical dataflows,* Eindhoven, 2002.

25]   R. Paschotta, "Encyclopedia of Laser Physics and Technology," [Online]. Available: http://www.rp-photonics.com. [Accessed 2 October 2011].

26]   K. A. Williams, M. G. Thompson and I. H. White, "Long-wavelength monolithic mode-locked diode lasers," *New Journal of Physics,* vol. 6, no. 179, 2004.

27]   M. S. Tahvili, Y. Barbarin, X. J. M. Leijtens, T. de Vries, E. Smalbrugge, J. Bolk, H. P. M. M. Ambrosius, M. K. Smit and E. A. J. M. Bente, "Directional control of optical power in integrated InP/InGaAsP extended cavity mode-locked ring lasers," *Optics Letters,* vol. 36, no. 13, 1 July 2011.

28]   J. Koeth, M. Fischer, M. Legge, J. Seufert, K. Rössner and H. Groninga, "DFB laser diodes for sensing applications using photoacoustic spectroscopy," *Journal of Physics,* 2010.

29]   T. F. Krauss, R. M. De La Rue, P. J. R. Laybourn, B. Vogele and C. R. Stanley, "Efficient semiconductor ring lasers made by a simple self-aligned fabrication process," *IEEE Journal of Selected Topics in Quantum Electronics,* vol. 1, no. 2, pp. 757-761, 1995.

30]   C. Schmidt-Langhorst, *Optical-Sampling of High Bit Rate Optical Data Signals,* Berlin, 2004.

31]   McGraw-Hill Companies, Inc., McGraw-Hill Dictionary of Scientific & Technical Terms, Sixth ed., McGraw-Hill, 2003.

32]   L. Douglas, "The Discrete Fourier Transform," *Journal of Object Technology,* vol. 9, no. 2, March-April 2010.

33]   K. L. Sala, G. A. Kenney-Wallace and G. E. Hall, "CW Autocorrelation Measurements of Picosecond Laser Pulses," *IEEE Journal of Quantum Electronics,* Vols. QE-16, no. 9, 1980.

34]   Anritsu, "Anritsu Home," December 2005. [Online]. [Accessed 04 12 2011].